

<sub>1</sub> Physics-Infused Reduced-Order Modeling for Analysis of  
<sub>2</sub> Ablating Hypersonic Thermal Protection Systems

<sub>3</sub>

<sub>4</sub> November 29, 2025

<sub>5</sub>

## Abstract

<sub>6</sub> This work presents a *physics-infused reduced-order modeling* (PIROM) framework  
<sub>7</sub> towards design, analysis, and optimization of non-decomposing ablating hypersonic  
<sub>8</sub> thermal protection systems (TPS), and is demonstrated via the modeling of transient  
<sub>9</sub> thermo-ablative responses of multi-layered hypersonic TPS. The PIROM architecture  
<sub>10</sub> integrates a *reduced-physics model* (RPM) as the building block, which is based on  
<sub>11</sub> the *lumped capacitance model* (LCM) coupled to a *surface recession model* (SRM).  
<sub>12</sub> The RPM provides a low-fidelity estimate of the thermo-ablative response of the TPS,  
<sub>13</sub> based on average temperatures and one-dimensional surface displacements. This RPM  
<sub>14</sub> is extended with data-driven hidden dynamics that are formulated via a systematic  
<sub>15</sub> coarse-graining approach rooted in the *Mori-Zwanzig* (MZ) formalism, and that are  
<sub>16</sub> learned from high-fidelity simulation data. Therefore, while the LCM and SRM capture  
<sub>17</sub> the dominant physics of the ablating TPS response, the correction terms compensate for  
<sub>18</sub> residual dynamics arising from higher-order non-linear interactions and temperature-  
<sub>19</sub> advection effects due to surface recession. The trained PIROM consistently achieves  
<sub>20</sub> errors of  $\approx 0.5\%$  for a wide range of extrapolative settings of design parameters involv-  
<sub>21</sub> ing time-and-space varying boundary conditions and SRM models, and improves by an  
<sub>22</sub> order of magnitude by the LCM alone. Moreover, the PIROM delivers RPM-level com-  
<sub>23</sub> putational costs, enabling evaluations that are two orders of magnitude faster than  
<sub>24</sub> the high-fidelity full-order model (FOM). These results demonstrate that PIROM ef-  
<sub>25</sub> fectively reconciles the trade-offs between accuracy, generalizability, and efficiency, pro-  
<sub>26</sub> viding a promising framework for optimizing multi-physical dynamical systems, such  
<sub>27</sub> as TPS, under diverse operating conditions.

<sub>28</sub>

# 1 Introduction

<sub>29</sub> At hypersonic speeds, aerospace vehicles experience extreme aero-thermo-dynamic environ-  
<sub>30</sub> ments that require specialized thermal protection systems (TPS) to shield internal sub-  
<sub>31</sub> structures, electronics, and possibly crew members from the intense aerodynamic heating.  
<sub>32</sub> The TPS is composed of ablating materials to withstand the high-energy physics – a high-  
<sub>33</sub> temperature-capable and fibrous material injected with a resin that fills the pore network  
<sub>34</sub> and strengthens the composite [1]. The TPS design promotes the exchange of mass through  
<sub>35</sub> thermal and chemical reactions (i.e., ablation), effectively mitigating heat transfer to the

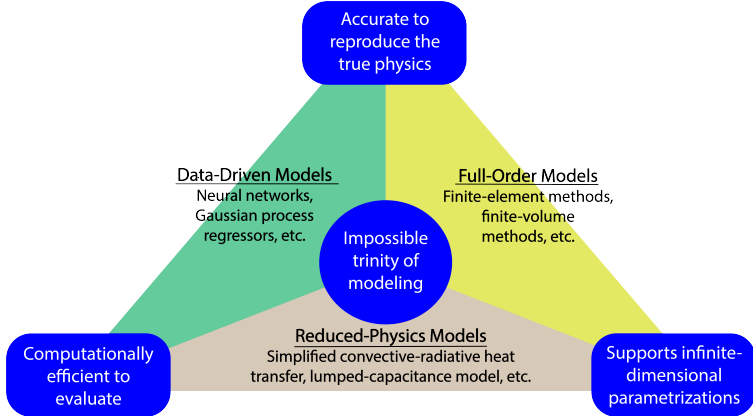


Figure 1: The impossible trinity of modeling: accuracy, generalizability, and efficiency.

sub-structures. As a result, accurate prediction for the ablating TPS response under extreme hypersonic heating becomes critical to ensuring survivability, performance, and safety of hypersonic vehicles.

Even with today’s advancements in computational resources and numerical methods, high-fidelity simulations of ablating TPS remains a formidable challenge, both theoretically and computationally. On the theoretical side, the thermo-chemical reactions, coupled with the irregular pore network structure and ablating boundaries, translate into complex non-linear equations governing multi-physical interactions across several spatio-temporal scales [1, 8]. On the computational side, numerical approaches based on finite-element (FEM) or finite-volume (FVM) methods yield systems of differential equations modeling the transient thermo-ablative response of the TPS [5]. The FEM discretizations lead to high-dimensional systems of equations, resulting in prohibitive computational costs for many-query applications such as design, optimization, uncertainty quantification, and real-time applications, where possibly thousands of model evaluations are required.

Reduced-order models (ROMs) have emerged as a promising approach to alleviate the computational costs of high-fidelity simulations [6, 11]. Ideally, a ROM should be: (1) accurate to reproduce high-fidelity solutions, (2) support continuous or infinite-dimensional design parameters such as geometrical shapes and material distributions, (3) be computationally efficient to evaluate to allow for fast turnaround times in design optimization. However, the above three capabilities usually form an *impossible trinity of modeling*, as illustrated in Fig. 1; building a ROM that achieves any two capabilities sacrifices the third.

The impossible trinity poses a significant challenge in the development of ROMs for the multi-disciplinary transient analysis and optimization of ablating TPS. Specifically, full-order models (FOMs), e.g., FEMs or FVMs, offer high accuracy and robust generalization over design spaces, but are computationally expensive to evaluate. Reduced-physics models (RPMs) – such as simplified convective-radiative heat transfer or engineering correlations – are low-dimensional models that achieve efficiency and broad applicability by ignoring higher-order non-linear effects. However, RPMs sacrifice accuracy for complex thermo-ablative responses due to the simplifications and assumptions inherent in their formulation, and it is generally not clear how to systematically leverage existing high-fidelity data to improve RPMs [19].

67 Lastly, data-driven ROMs, such as Gaussian Process Regression (GPR) [16], Neural Net-  
68 works (NNs), and neural ordinary differential equations (NODEs) [3], can provide accurate  
69 and computationally-efficient approximations of high-fidelity models for complex thermo-  
70 ablative responses. However, these data-centric approaches often demand extensive high-  
71 fidelity data for training, do not necessarily satisfy fundamental physical constraints or con-  
72 servation laws, and thus do not generalize well to the design spaces outside the training [17].  
73 For example, our previous work demonstrated that NODEs trained on high-fidelity data of  
74 non-ablating TPS failed to generalize when subjected to boundary conditions and material  
75 models outside the training set [18].

76 This work presents the extension of the *physics-infused reduced-order modeling* (PIROM)  
77 framework to include effects of ablation for TPS applications, previously ignored in Ref. [18].  
78 Specifically, the PIROM is demonstrated for the transient thermo-ablative response of multi-  
79 layered hypersonic TPS. The PIROM is a non-intrusive framework that combines the strengths  
80 of physics-based models with machine learning to formulate and train ROMs for parametrized  
81 non-linear dynamical systems. The backbone of the PIROM is the physics-based component,  
82 i.e., the RPM, which in this work is composed of: (1) a *lumped capacitance model* (LCM)  
83 to model the average heat transfer within the TPS layers, and (2) a *surface recession model*  
84 (SRM) to model one-dimensional surface ablation.

85 Leveraging the *Mori-Zwanzig* (MZ) formalism [15, 14, 13], the RPM is rigorously ex-  
86 tended with data-driven hidden dynamics to account for the missing physics in the LCM,  
87 which are learned from high-fidelity data. The hidden dynamics enable higher predictive  
88 accuracy of the PIROM when subjected to complex boundary conditions and SRM model  
89 variations. For the TPS problem, the MZ approach produces a sufficiently simple model  
90 form while maintaining the physical consistency of the PIROM, as well as the dependence  
91 on design parameters. Thus, the PIROM aims to solve the ITM by leveraging the gen-  
92 eralizability and computational efficiency of RPMs, while incorporating the accuracy and  
93 adaptability of data-driven extensions. More importantly, the PIROM formulation provides  
94 a general methodology for developing PIROMs for other multi-physics problems.

95 The specific objectives of this work are summarized as follows:

- 96 1. Extend the previous PIROM formulation in Ref. [18] to model transient thermo-  
97 ablative response of multi-layered hypersonic TPS through a systematic coarse-graining  
98 procedure based on the Mori-Zwanzig formalism.
- 99 2. Benchmark the accuracy, generalizability, and computational accelerations of the PIROM  
100 against the RPM and the high-fidelity FEM solutions of ablating TPS, thus quanti-  
101 fying the PIROM’s capabilities to solve the ITM in complex multi-physical non-linear  
102 dynamical systems.

## 103 2 Modeling of Thermal Protection Systems

104 This section presents the problem of modeling the transient thermo-ablative response of a  
105 non-decomposing TPS, subjected to extreme hypersonic heating. Two different but math-  
106 ematically connected solution strategies are provided: (1) a high-fidelity full-order model

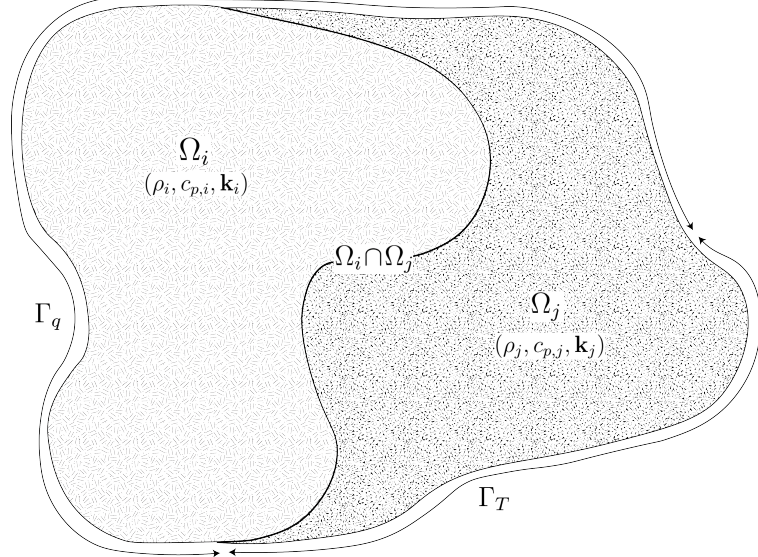


Figure 2: General domain  $\Omega$  with prescribed Neumann and Dirichlet boundary conditions on  $\Gamma_q$  and  $\Gamma_T$ . Mesh displacement  $w(x, t)$  occurs on the  $\Gamma_q$  boundary.

107 (FOM) based on a finite element method (FEM), and (2) a RPM based on a *lumped capacitance model* (LCM) coupled with a one-dimensional *surface recession model* (SRM). The  
108 FOM is computationally expensive but provides the highest fidelity, while the RPM is com-  
109 putationally efficient but has low predictive fidelity. However, both models are physically  
110 consistent to high-dimensional design variables. The following discussion presents the TPS  
111 modeling problem and the FOM and RPM solution strategies.  
112

## 113 2.1 Governing Equations

114 The multi-physics of a non-decomposing ablating TPS under a hypersonic boundary layer  
115 involves the *energy equation* for heat conduction inside the TPS, and the *pseudo-elasticity*  
116 *equation* for mesh motion due to surface recession. The coupling between these two equations  
117 occurs at the heated boundary, where the surface temperature drives the surface recession  
118 velocity, which appears as an advection term in the energy equation. The governing PDEs  
119 are described as follows.

### 120 2.1.1 Energy Equation

121 Consider a generic domain  $\Omega \subset \mathbb{R}^d$ ,  $d = 2$  or  $3$ , illustrated in Fig. 2. Let  $\partial\Omega = \Gamma_q \cup \Gamma_T$   
122 and  $\Gamma_q \cap \Gamma_T = \emptyset$ , where a Neumann  $q_b(x, t)$  boundary condition is prescribed on the heated  
123 boundary  $\Gamma_q$ , and represents the surface exposed to the hypersonic boundary layer. The  
124 Dirichlet  $T_b(x, t)$  boundary condition is prescribed on the boundary  $\Gamma_T$ . The TPS is divided  
125 into  $N$  non-overlapping components  $\{\Omega_i\}_{i=1}^N$ , as illustrated in Fig. 2 for  $N = 2$ . The  $i$ -th  
126 component  $\Omega_i$  is associated with material properties  $(\rho_i, c_{p,i}, \mathbf{k}_i)$ , which are continuous within  
127 one component, and can be discontinuous across two neighboring components.

128 Over the time domain  $\mathcal{T} = [t_0, t_f]$ , the energy equation describes the transient heat

<sup>129</sup> conduction inside the TPS,

$$\rho c_p \left( \frac{\partial T}{\partial t} + \tilde{\mathbf{v}}(x, t) \cdot \nabla T \right) - \nabla \cdot (\mathbf{k} \nabla T) = 0, \quad t \in \mathcal{T}, x \in \Omega \quad (1a)$$

$$-\mathbf{k} \nabla T \cdot \mathbf{n} = q_b(x, t), \quad t \in \mathcal{T}, x \in \Gamma_q \quad (1b)$$

$$T(x, t) = T_b(x, t), \quad t \in \mathcal{T}, x \in \Gamma_T \quad (1c)$$

$$T(x, 0) = T_0(x), \quad x \in \Omega \quad (1d)$$

<sup>130</sup> where  $\rho$ ,  $c_p$ , and  $\mathbf{k} \in \mathbb{R}^{d \times d}$  are the constant density, heat capacity, and thermal conductivity, respectively. Note that our prior work has applied the PIROM to TPS problems <sup>131</sup> with temperature-varying material properties [18]. In Eq. (1) the  $\rho c_p \frac{\partial T}{\partial t}$  term includes the <sup>132</sup> unsteady energy storage,  $\rho c_p \tilde{\mathbf{v}}(x, t) \cdot \nabla T$  includes the temperature advection due to ablation, <sup>133</sup> and  $\nabla \cdot (\mathbf{k} \nabla T)$  includes the heat conduction. <sup>134</sup>

<sup>135</sup> An Arbitrary Lagrangian-Eulerian (ALE) description is used to account for mesh motion <sup>136</sup> due to surface recession. The relative velocity of the material  $\tilde{\mathbf{v}}(x, t)$  with respect to the <sup>137</sup> mesh is,

$$\tilde{\mathbf{v}}(x, t) = \mathbf{v}_s(x, t) - \mathbf{v}_m(x, t) \quad (2)$$

<sup>138</sup> where  $\mathbf{v}_s(x, t)$  and  $\mathbf{v}_m(x, t)$  are the physical material velocity and mesh velocity, respectively. <sup>139</sup> In this work, the physical material velocity is assumed to be zero, i.e.,  $\mathbf{v}_s(x, t) = \mathbf{0}$ , and thus <sup>140</sup> the relative velocity is simply the negative of the mesh velocity,  $\tilde{\mathbf{v}}(x, t) = -\mathbf{v}_m(x, t)$ . The <sup>141</sup> advection term in Eq. (1a) thus captures the effect of temperature advection due to mesh <sup>142</sup> motion, and the governing equation for the mesh velocity is provided next.

### <sup>143</sup> 2.1.2 Pseudo-Elasticity Equation

<sup>144</sup> At some time  $t$ , the mesh displacement field  $\mathbf{d}_m \in \mathbb{R}^d$  is described by the steady-state <sup>145</sup> pseudo-elasticity equation, which models the mesh as a fictitious elastic solid that deforms <sup>146</sup> according to the prescribed Dirichlet boundary conditions. The mesh velocities are obtained <sup>147</sup> by differentiating the mesh displacements with respect to time, i.e.,  $\mathbf{v}_m(x, t) = \dot{\mathbf{d}}_m$ , which <sup>148</sup> appear in the advection term of the energy equation in Eq. (1a) and is approximated using <sup>149</sup> finite differences in the coupled simulation. The governing equation for mesh displacements <sup>150</sup> is,

$$\nabla \cdot \boldsymbol{\sigma}(\mathbf{d}_m) = \mathbf{0}, \quad \forall x \in \Omega \quad (3a)$$

$$\mathbf{d}_m(x, t) = \mathbf{d}_q(x, t), \quad \forall x \in \Gamma_q \quad (3b)$$

$$\mathbf{d}_m(x, t) = \mathbf{0}, \quad \forall x \in \Gamma_T \quad (3c)$$

$$\mathbf{d}_m(x, 0) = \mathbf{0}, \quad \forall x \in \Omega \quad (3d)$$

<sup>151</sup> where the stress tensor  $\boldsymbol{\sigma}$  is related to the strain tensor  $\boldsymbol{\epsilon}(\mathbf{d}_m)$  through Hooke's law,

$$\boldsymbol{\sigma}(\mathbf{d}_m) = \mathbb{D} : \boldsymbol{\epsilon}(\mathbf{d}_m)$$

<sup>152</sup> where  $\mathbb{D}$  is the fourth-order positive definite elasticity tensor, and ":" is the double contraction <sup>153</sup> of the full-order tensor  $\mathbb{D}$  with the second-order tensor  $\boldsymbol{\epsilon}$ . In this work, the standard

<sup>154</sup> isotropic case is considered, where  $\mathbb{D}$  is fully described by two Lamé parameters  $\lambda$  and  $\mu$   
<sup>155</sup> arbitrarily. The symmetric strain tensor  $\boldsymbol{\epsilon}$  measures the deformation of the mesh due to  
<sup>156</sup> displacements  $\mathbf{d}_m(x, t)$ , and is defined as,

$$\boldsymbol{\epsilon}(\mathbf{d}_m) = \frac{1}{2} (\nabla \mathbf{d}_m + \nabla \mathbf{d}_m^\top)$$

<sup>157</sup> The “material” properties for the mesh are chosen to tailor the mesh deformation, and need  
<sup>158</sup> not represent the actual material being modeled [1].

<sup>159</sup> The boundary conditions  $\mathbf{d}_q$  and  $\mathbf{d}_T = \mathbf{0}$  are Dirichlet-type on the heated  $\Gamma_q$  and unheated  
<sup>160</sup>  $\Gamma_T$  boundaries, respectively, and the initial mesh displacement is set to zero as in Eq. (3d).  
<sup>161</sup> The surface velocity due to ablation is a function of the surface temperature  $T_q(x, t)$  for  
<sup>162</sup>  $x \in \Gamma_q$ . For the  $i$ -th material component, the mesh velocity is imposed based on the following  
<sup>163</sup> relation,

$$\hat{\mathbf{n}} \cdot \mathbf{v}_m(x, t) = f_i(T_q(x, t)), \quad x \in \Gamma_{q,i} \quad (4)$$

<sup>164</sup> where  $\Gamma_q = \cup_{i=1}^{\tilde{N}} \Gamma_{q,i}$  with  $\Gamma_{q,i}$  as the portion of the heated boundary that belongs to the  
<sup>165</sup>  $i$ -th ablative component,  $\tilde{N}$  is the number of ablative components with  $\tilde{N} \leq N$ ,  $\hat{\mathbf{n}}$  is the  
<sup>166</sup> unit normal vector, and  $f_i$  is a material-dependent function obtained from tabulated data,  
<sup>167</sup> commonly referred to as a B' table [1]. The B' table provides a model for the recession  
<sup>168</sup> velocity as a function of the surface temperature, and is pre-computed based on high-fidelity  
<sup>169</sup> simulations or physical experiments for a one-dimensional slab of materials, and is indepen-  
<sup>170</sup> dent of the TPS geometry. Provided the surface velocity, the boundary condition in Eq. (5)  
<sup>171</sup> for the mesh displacements are computed by integrating the surface velocity over time,

$$\mathbf{d}_q(x, t) = \int_0^t \mathbf{v}_m(x, \tau) d\tau, \quad x \in \Gamma_q \quad (5)$$

## <sup>172</sup> 2.2 Full-Order Model: Finite-Element Method

<sup>173</sup> The transient thermo-ablative response of the TPS is modeled using a high-fidelity FOM  
<sup>174</sup> based on FEM. The governing PDEs – namely, the energy equation in Eq. (1) and the  
<sup>175</sup> pseudo-elasticity equation in Eq. (3) – are numerically solved using the Aria multi-physics  
<sup>176</sup> code developed at Sandia National Laboratories [2]. While the standard practice in multi-  
<sup>177</sup> dimensional ablative TPS solvers is to employ continuous Galerkin FEM for both the energy  
<sup>178</sup> and mesh-motion equations, this work adopts a *discontinuous Galerkin* FEM (DG-FEM)  
<sup>179</sup> formulation for the energy equation. The DG-FEM formulation is mainly for theoretical  
<sup>180</sup> convenience to support the model-order reduction procedures in the subsequent PIROM  
<sup>181</sup> derivations; equivalence between DG and standard FEM is noted upon their convergence.  
<sup>182</sup> The following discussion presents the numerical solution of both governing equations, as well  
<sup>183</sup> as the coupling scheme between them.

<sup>184</sup> **Energy Equation** Consider a conforming mesh partition of the TPS domain into  $M$   
<sup>185</sup> elements  $\{E_i\}_{i=1}^M$ , where each element belongs exactly to one TPS component  $\Omega_j$ . Let  $e_{ij}$   
<sup>186</sup> denote the interface between neighboring elements  $E_i$  and  $E_j$ , and let  $e_{iq}$  and  $e_{iT}$  denote  
<sup>187</sup> the portions of the element boundary on the Neumann  $\Gamma_q$  and Dirichlet  $\Gamma_T$  boundaries,

188 respectively. The quantity  $|e|$  denotes the length ( $d = 2$ ) or area ( $d = 3$ ) of a component  
 189 boundary  $e$ . For the  $i$ -th element, use a set of  $P$  trial functions, such as polynomials, to  
 190 represent the temperature distribution,

$$T_i(x, t) = \sum_{l=1}^P \phi_l^i(x) u_l^i(t) \equiv \boldsymbol{\phi}_i^\top(x) \mathbf{u}_i(t), \quad i = 1, 2, \dots, M \quad (6)$$

191 Applying the DG variational formulation, incorporating the numerical fluxes across all ele-  
 192 ment interfaces, and assembling over the mesh yields the semi-discrete system of ODEs,

$$\mathbf{A}\dot{\mathbf{u}} = [\mathbf{B} + \mathbf{C}(\mathbf{u})] \mathbf{u} + \mathbf{f}(t) \quad (7)$$

193 where  $\mathbf{u} = [\mathbf{u}_1, \mathbf{u}_2, \dots, \mathbf{u}_M]^\top \in \mathbb{R}^{MP}$  includes all the DG variables,  $\mathbf{f} \in \mathbb{R}^{MP}$  is the external  
 194 forcing, and the system matrices  $\mathbf{A}$ ,  $\mathbf{B}$ , and  $\mathbf{C}$  are the matrices due to heat capacity, heat  
 195 conduction, and temperature advection due to mesh motion, respectively. Note that the  
 196 advection matrix  $\mathbf{C}(\mathbf{u})$  is a function of the mesh velocity  $\mathbf{v}_m$ , which in turn is a function  
 197 of temperature through the boundary condition in Eq. (4); this is the main source of non-  
 198 linearity in the current TPS problem. A detailed derivation of Eq. (7) and their matrices is  
 199 provided in Appendix A.

200 **Pseudo-Elasticity Equation** The *steady pseudo-elasticity equation* is spatially discretized  
 201 using the standard Galerkin FEM method on a structured mesh with quadrilateral elements.  
 202 Define the scalar basis functions  $\{\psi_j(x)\}_{j=1}^Q$  associated with the global displacement degrees  
 203 of freedom  $\{\mathbf{d}_j\}_{j=1}^Q$  where  $Q$  is the total number of nodes in the mesh. At time  $t$ , the mesh  
 204 displacement field  $\mathbf{d}_m(x)$  is approximated as,

$$\mathbf{d}_m(x) \approx \sum_{j=1}^Q \psi_j(x) \mathbf{d}_j \quad (8)$$

205 Substituting into the weak form of Eq. (3a), the following linear system of equations is  
 206 obtained for the nodal displacements at each time step,

$$\mathbf{K}\mathbf{d} = \mathbf{g} \quad (9)$$

207 where  $\mathbf{d}$  is the global displacement vector,  $\mathbf{K} \in \mathbb{R}^{dQ \times dQ}$  the global stiffness matrix for a  
 208  $d$ -dimensional problem, defined by the volume integrals over the domain  $\Omega$  provided the  
 209 elasticity tensor  $\mathbb{D}$ , and  $\mathbf{g}$  is the global force vector due to the Dirichlet boundary conditions  
 210 on the heated  $\Gamma_q$  and unheated  $\Gamma_T$  boundaries.

211 **Coupled Full-Order Model** The temperature-dependent mesh motion on the heated  
 212 boundary  $\Gamma_q$  naturally defines a two-way coupling scheme between the energy and pseudo-  
 213 elasticity FEM models. At each time step, the coupling proceeds as: (1) *boundary dis-  
 214 placement update*, (2) *mesh displacement solve*, and (3) *thermal solve with mesh-induced  
 215 advection*. In the boundary displacement update, the surface temperature  $T_q(x, t)$  on the

216 heated boundary  $\Gamma_q$  is used to evaluate the recession velocity through the B' table as in  
 217 Eq. (4). Integrating this velocity over the time step provides the prescribed boundary dis-  
 218 placement  $\mathbf{d}_q(x, t)$  in Eq. (5). In the mesh displacement solve, the pseudo-elasticity equation  
 219 in Eq. (9) is solved to obtain the mesh displacement field  $\mathbf{d}_m(x)$  based on the updated bound-  
 220 ary displacements. A finite-difference approximation is then applied to compute the mesh  
 221 velocity  $\mathbf{v}_m(x, t) = \dot{\mathbf{d}}_m$  based on history of displacement fields. In the thermal FEM solve  
 222 with mesh-induced advection, the mesh velocity field enters the advection operator  $\mathbf{C}(\mathbf{u})$  in  
 223 the semi-discrete energy equation in Eq. (7). The energy equation is then advanced using  
 224 an implicit-time integration scheme until the final time  $t_f$  is reached.

## 225 2.3 Reduced-Physics Model

226 The RPM for predicting the response of the ablating TPS consists of two components: (1)  
 227 *surface recession model* (SRM) and a *lumped capacitance model* (LCM). The SRM provides  
 228 a relation between the surface temperature and *one-dimensional* surface recession veloc-  
 229 ity based on pre-computed B' tables for the material, enabling the computation of *one-*  
 230 *dimensional* surface displacements. Provided the geometry changed induced by the surface  
 231 recession, the LCM predicts the average temperature inside each component of the TPS,  
 232 which are in turn used as low-fidelity estimates for the surface temperatures required by the  
 233 SRM. Therefore, the SRM and LCM are coupled to define the RPM, providing low-fidelity  
 234 estimates for temperatures and surface recessions of the ablating TPS.

### 235 2.3.1 Surface Recession Model

236 The mesh displacements  $\mathbf{d}$  are constrained to be *one-dimensional* on the heated boundary  
 237  $\Gamma_q$ , i.e.,  $w_i(x, t) = \mathbf{d}(x, t) \cdot \hat{\mathbf{n}}_i$ , where  $\hat{\mathbf{n}}_i$  is the unit normal vector on the heated boundary  
 238  $\Gamma_{q,i}$ . Displacements perpendicular to  $\hat{\mathbf{n}}_i$  for  $i = 1, \dots, \tilde{N}$  are assumed to be small and thus  
 239 neglected. Let  $\mathbf{w} = [w_1, w_2, \dots, w_{\tilde{N}}]^\top \in \mathbb{R}^{\tilde{N}}$  include the one-dimensional displacements for  
 240 the  $\tilde{N}$  ablating components on the heated boundary, where  $\tilde{N} \leq N$ . Then the SRM is  
 241 described as,

$$\dot{\mathbf{w}} = \boldsymbol{\Xi} \mathbf{u} - \tilde{\mathbf{f}} \quad (10)$$

242 where  $\boldsymbol{\Xi} = \text{diag}(\alpha_1, \dots, \alpha_{\tilde{N}})$  and  $\tilde{\mathbf{f}} = (\alpha_1 u_{0,1}, \dots, \alpha_{\tilde{N}} u_{0,\tilde{N}})^\top$ . The constants  $\alpha_i$  are small  
 243 material-dependent parameters, determined from the B' table, and  $u_{0,i}$  is the constant initial  
 244 temperature of the ablative component. The SRM provides a relation between the surface's  
 245 temperature and recession velocity, based on pre-computed B' tables for the material.

### 246 2.3.2 Lumped Capacitance Model

247 A general form of the LCM is provided in this section; details regarding the derivation for  
 248 the four-component TPS used in the results section are provided in Appendix A. Let  $\Omega$  be  
 249 partitioned into  $N$  non-overlapping components  $\{\Omega_i\}_{i=1}^N$ , as illustrated in Fig. 2 for  $N = 2$ .  
 250 The domain  $\Omega$  is a function of the surface displacements  $\mathbf{w}$ , and thus the geometry of each  
 251 component  $\Omega_i$  is time-dependent. The LCM predicts the temporal variation of average  
 252 temperatures in multiple shape-varying interconnected components [9]. From a point of

253 sview of energy conservation, the LCM leads to the following system of first-order ODEs for  
 254 the average temperatures in the components,

$$\bar{\mathbf{A}}(\mathbf{w})\dot{\bar{\mathbf{u}}} = \bar{\mathbf{B}}(\mathbf{w})\bar{\mathbf{u}} + \bar{\mathbf{f}}(t) \quad (11)$$

255 Where the states and inputs,

$$\bar{\mathbf{u}} = [\bar{u}_1, \bar{u}_2, \dots, \bar{u}_N]^\top \in \mathbb{R}^N, \quad \bar{\mathbf{f}} = [\bar{f}_1, \bar{f}_2, \dots, \bar{f}_N]^\top \in \mathbb{R}^N \quad (12)$$

256 include the average temperatures  $\bar{\mathbf{u}}$  and spatially-integrated inputs  $\bar{\mathbf{f}}$  for the  $N$  components.  
 257 For  $i, j = 1, 2, \dots, N$  the  $(i, j)$ -th elements of the  $\bar{\mathbf{A}} \in \mathbb{R}^{N \times N}$ ,  $\bar{\mathbf{B}} \in \mathbb{R}^{N \times N}$ , and  $\bar{\mathbf{f}} \in \mathbb{R}^N$   
 258 matrices are given by,

$$\bar{A}_i = \begin{cases} \int_{\Omega_i} \rho c_p d\Omega_i, & i = j \\ 0, & i \neq j \end{cases}, \quad \bar{B}_{ij} = \begin{cases} \sum_{j \in \mathcal{N}_i \cup \{T_b\}} \bar{B}_{ij}^i, & i = j \\ \bar{B}_{ij}^{(j)}, & i \neq j \end{cases}, \quad (13a)$$

$$\mathbf{f}_i = \begin{cases} |e_{iq}| \bar{q}_i + \frac{|e_{iT}|}{R_i} \bar{T}_i, & i = j \\ 0, & i \neq j \end{cases} \quad (13b)$$

259 where,

$$\bar{q}_i = \frac{1}{|e_{iq}|} \int_{e_{iq}} q_b de_{iq}, \quad \bar{T}_i = \frac{1}{|e_{iT}|} \int_{e_{iT}} T_b de_{iT}, \quad \bar{B}_{ij}^i = -\frac{|e_{ij}|}{R_{ij}}, \quad \bar{B}_{ij}^j = \frac{|e_{ij}|}{R_{ij}} \quad (14)$$

260 where  $R_{ij}$  is the equivalent thermal resistance between two neighboring components  $\Omega_i$  and  
 261  $\Omega_j$ , and  $R_i$  is the thermal resistance between component  $\Omega_i$  and the Dirichlet boundary.  
 262 Note that the heat capacitances and thermal resistances are computed based on the current  
 263 geometry of each component, which is a function of  $\mathbf{w}$  provided by the SRM.

### 264 2.3.3 Thermo-Ablative Reduced-Physics Model

265 The SRM and LCM are combined to define the RPM for predicting the thermo-ablative  
 266 response of the TPS under hypersonic boundary layers. Specifically, the RPM is defined as  
 267 the LCM as in Eq. (11), where the *geometry-dependent* matrices  $\tilde{\mathbf{A}}$  and  $\tilde{\mathbf{B}}$  are updated at  
 268 each time step based on the current displacements  $\mathbf{w}$  provided by the SRM. The RPM is  
 269 formally stated as,

$$\tilde{\mathbf{A}}(\mathbf{s})\dot{\tilde{\mathbf{s}}} = \tilde{\mathbf{B}}(\mathbf{s})\mathbf{s} + \tilde{\mathbf{F}}(t) \quad (15a)$$

$$\tilde{\mathbf{z}} = \mathbf{s} \quad (15b)$$

270 where the state  $\mathbf{s} = [\bar{\mathbf{u}}, \mathbf{w}]^\top \in \mathbb{R}^{N+\tilde{N}}$  includes the *average temperature* and *one-dimensional*  
 271 *surface displacements*, and  $\tilde{N}$  is the number of ablating components with  $\tilde{N} \leq N$ . Moreover,  
 272 the observables are defined as  $\mathbf{z} = [\bar{\mathbf{u}}, \mathbf{w}]^\top \in \mathbb{R}^{N+\tilde{N}}$ . The matrices are given as,

$$\tilde{\mathbf{A}}(\mathbf{s}) = \begin{bmatrix} \bar{\mathbf{A}}(\mathbf{s}) & \mathbf{0} \\ \mathbf{0} & \mathbf{I} \end{bmatrix}, \quad \tilde{\mathbf{B}}(\mathbf{s}) = \begin{bmatrix} \bar{\mathbf{B}}(\mathbf{s}) & \mathbf{0} \\ \Xi & \mathbf{0} \end{bmatrix}, \quad \tilde{\mathbf{F}}(t) = \begin{bmatrix} \bar{\mathbf{f}}(t) \\ -\tilde{\mathbf{f}} \end{bmatrix} \quad (16)$$

273 In the matrices  $\tilde{\mathbf{A}}$  and  $\tilde{\mathbf{B}}$ , the surface displacements  $\mathbf{w}$  are used to define the dimensions for  
274 the  $\Omega_i$  component used in Eqs. (13) and (14), thus effectively coupling the LCM and SRM.

## 275 2.4 Summary of Modeling Approaches

276 The FOM (i.e., FEM) and RPM (i.e., LCM with SRM) are two different but mathematically  
277 connected solution strategies. Particularly, the LCM in Eq. (11) not only resembles the  
278 functional form of the DG model in Eq. (7), but can be viewed as a special case of the latter,  
279 where the mesh partition is extremely coarse, and the trial and test functions are piece-wise  
280 constants. This removes all spatial variations within each component, and neglects advection  
281 effects due to mesh motion.

282 For example, consider the case where each component  $\Omega_i$  is treated as one single element,  
283 and each element employs one constant basis function  $\phi_i = 1$ . The DG-FEM model for the  
284  $i$ -th component simplifies to the scalar ODE,

$$\mathbf{A}^i = \bar{A}_i, \quad \mathbf{C}^i = 0, \quad \mathbf{B}_{ij}^i = -\sigma|e_{ij}|, \quad \mathbf{B}_{ij}^j = \sigma|e_{ij}|, \quad \mathbf{f}_i = |e_{iq}|\bar{q}_i + \sigma|e_{iT}|\bar{T}_i \quad (17)$$

285 Clearly, the LCM is a coarse zeroth-order DG model with the inverse of thermal resistance  
286 chosen as the element-wise penalty factors. Or conversely, the DG model is a refined version  
287 of LCM via  $hp$ -adaptation.

288 The FOM and RPM represent two extremes in the modeling fidelity and computational  
289 cost spectrum. On one hand, the FOM is the most accurate but computationally expensive  
290 to evaluate due to the fine mesh discretizations for both the temperature and displacement  
291 fields, leading to possibly millions of state variables. On the other hand, the RPM considers  
292 only the average temperature of the material, from which the displacements are obtained by  
293 integrating the velocity. The coarsened representation of the temperature field significantly  
294 reduces the number of state variables to only a few per component, and thus reducing the  
295 computational cost. However, this sacrifices local temperature information that becomes  
296 critical to properly capture higher-order effects due to mesh motion and thermal gradients  
297 within each component. Thus, neither the FOM nor the RPM is an universal approach for  
298 real-world analysis, design, and optimization tasks for ablating TPS, where thousands of  
299 high-fidelity model evaluations may be necessary. This issue motivates the development of  
300 the PIROM, which can achieve the fidelity of FOM at a computational cost close to the  
301 RPM, while maintaining the generalizability to model parameters.

## 302 3 Physics-Infused Reduced-Order Modeling

303 The formulation of PIROM for ablating TPS starts by connecting the FOM, i.e., the DG-  
304 FEM, and the RPM, i.e., the LCM, via a coarse-graining procedure. This procedure pin-  
305 points the missing dynamics in the LCM when compared to DG-FEM. Subsequently, the  
306 Mori-Zwanzig (MZ) formalism is employed to determine the model form for the missing dy-  
307 namics in PIROM. Lastly, the data-driven identification of the missing dynamics in PIROM  
308 is presented.

### 309 3.1 Deriving the Reduced-Physics Model via Coarse-Graining

310 The subsequent coarse-graining formulation is performed on the DG-FEM in Eq. (7) to  
 311 derive the LCM in Eq. (11). This process constraints the trial function space of a full-  
 312 order DG model to a subset of piece-wise constants, so that the variables  $\mathbf{u}$ , matrices  $\mathbf{A}$ ,  
 313  $\mathbf{B}$ , and  $\mathbf{C}$ , and forcing vector  $\mathbf{f}$  are all approximated using a single state associated to the  
 314 average temperature. Note that the coarse-graining is exclusively performed on the thermal  
 315 dynamics, as it is the surface temperature that drives the one-dimensional recession via  
 316 the SRM. Hence, the coarse-graining of the mesh dynamics is not included in the following  
 317 procedure.

#### 318 3.1.1 Coarse-Graining of States

319 Consider a DG model as in Eq. (7) for  $M$  elements and an LCM as in Eq. (11) for  $N$   
 320 components; clearly  $M \gg N$ . Let  $\mathcal{V}_j = \{i | E_i \in \Omega_j\}$  be the indices of the elements belonging  
 321 to the  $j$ -th component, so  $E_i \in \Omega_j$  for all  $i \in \mathcal{V}_j$ . The number of elements in the  $j$ -th  
 322 component is  $|\mathcal{V}_j|$ . The average temperature on  $\Omega_j$  is,

$$323 \bar{u}_j = \frac{1}{|\Omega_j|} \sum_{i \in \mathcal{V}_j} \int_{E_i} \boldsymbol{\phi}^{(i)}(x)^T \mathbf{u}^{(i)} d\Omega = \frac{1}{|\Omega_j|} \sum_{i \in \mathcal{V}_j} |E_i| \boldsymbol{\varphi}_i^{j\top} \mathbf{u}^{(i)}, \quad j = 1, 2, \dots, N \quad (18)$$

323 where  $|\Omega_j|$  and  $|E_i|$  denote the area ( $d = 2$ ) or volume ( $d = 3$ ) of component  $j$  and element  
 324  $i$ , respectively. The orthogonal basis functions are defined as  $\boldsymbol{\varphi}_i^{j\top} = [1, 0, \dots, 0]^\top \in \mathbb{R}^P$ .

325 Conversely, given the average temperatures of the  $N$  components,  $\bar{\mathbf{u}}$ , the states of an  
 326 arbitrary element  $E_i$  is written as,

$$327 \mathbf{u}^{(i)} = \sum_{k=1}^N \boldsymbol{\varphi}_i^k \bar{u}_k + \delta \mathbf{u}^{(i)}, \quad i = 1, 2, \dots, M \quad (19)$$

327 where  $\boldsymbol{\varphi}_i^k = 0$  if  $i \notin \mathcal{V}_k$ , and  $\delta \mathbf{u}^{(i)}$  represents the deviation from the average temperature and  
 328 satisfies the orthogonality condition  $\boldsymbol{\varphi}_i^{k\top} \delta \mathbf{u}^{(i)} = 0$  for all  $k$ .

329 Equations Eqs. (18) and (19) are combined and written in matrix form as,

$$329 \bar{\mathbf{u}} = \boldsymbol{\Phi}^+ \mathbf{u}, \quad \mathbf{u} = \boldsymbol{\Phi} \mathbf{u} + \delta \mathbf{u} \quad (20)$$

330 where  $\boldsymbol{\Phi} \in \mathbb{R}^{MP \times N}$  is a matrix of  $M \times N$  blocks, with the  $(i, j)$ -th block as  $\boldsymbol{\varphi}_i^j$ ,  $\boldsymbol{\Phi}^+ \in \mathbb{R}^{N \times MP}$   
 331 is the left inverse of  $\boldsymbol{\Phi}$ , with the  $(i, j)$ -th block as  $\boldsymbol{\varphi}_i^{j+} = \frac{|E_i|}{|\Omega_j|} \boldsymbol{\varphi}_i^{j\top}$ , and  $\delta \mathbf{u}$  is the collection of  
 332 deviations. By their definitions,  $\boldsymbol{\Phi}^+ \boldsymbol{\Phi} = \mathbf{I}$  and  $\boldsymbol{\Phi}^+ \delta \mathbf{u} = \mathbf{0}$ .

#### 333 3.1.2 Coarse-Graining of Dynamics

334 The dependence of the matrices with respect to the displacements  $\mathbf{w}$  is dropped to isolate  
 335 the analysis based on coarsened variables. Consider a function of states in the form of  
 336  $\mathbf{M}(\mathbf{u}) \mathbf{g}(\mathbf{u})$ , where  $\mathbf{g} : \mathbb{R}^{MP} \rightarrow \mathbb{R}^{MP}$  is a vector-valued function, and  $\mathbf{M} : \mathbb{R}^{MP} \rightarrow \mathbb{R}^{p \times MP}$   
 337 is a matrix-valued function with an arbitrary dimension  $p$ . Define the projection matrix

<sup>338</sup>  $\mathbf{P} = \Phi\Phi^+$  and the projection operator  $\mathcal{P}$  as,

$$\begin{aligned}\mathcal{P}[\mathbf{M}(\mathbf{u})\mathbf{g}(\mathbf{u})] &= \mathbf{M}(\mathbf{P}\mathbf{u})\mathbf{g}(\mathbf{P}\mathbf{u}) \\ &= \mathbf{M}(\Phi\bar{\mathbf{u}})\mathbf{g}(\Phi\bar{\mathbf{u}})\end{aligned}\quad (21)$$

<sup>339</sup> so that the resulting function depends only on the average temperatures  $\bar{\mathbf{u}}$ . Correspondingly,  
<sup>340</sup> the residual operator  $\mathcal{Q} = \mathcal{I} - \mathcal{P}$ , and  $\mathcal{Q}[\mathbf{M}(\mathbf{u})\mathbf{g}(\mathbf{u})] = \mathbf{M}(\mathbf{u})\mathbf{g}(\mathbf{u}) - \mathbf{M}(\Phi\bar{\mathbf{u}})\mathbf{g}(\Phi\bar{\mathbf{u}})$ . When  
<sup>341</sup> the function is not separable, the projection operator is simply defined as  $\mathcal{P}[\mathbf{g}(\mathbf{u})] = \mathbf{g}(\mathbf{P}\mathbf{u})$ .

<sup>342</sup> Subsequently, the operators defined above are applied to coarse-grain the dynamics. First,  
<sup>343</sup> write the DG-FEM in Eq. (7) as,

$$\dot{\mathbf{u}} = \mathbf{A}^{-1}\mathbf{B}\mathbf{u} + \mathbf{A}^{-1}\mathbf{C}(\mathbf{u})\mathbf{u} + \mathbf{A}^{-1}\mathbf{f}(t) \quad (22)$$

<sup>344</sup> and multiply both sides by  $\Phi^+$  to obtain,

$$\Phi^+\dot{\mathbf{u}} = \Phi^+(\Phi\bar{\mathbf{u}} + \delta\dot{\mathbf{u}}) = \dot{\bar{\mathbf{u}}} = \Phi^+\mathbf{r}(\mathbf{u}, t) \quad (23)$$

<sup>345</sup> Apply the projection operator  $\mathcal{P}$  and the residual operator  $\mathcal{Q}$  to the right-hand side to obtain,

$$\dot{\bar{\mathbf{u}}} = \mathcal{P}[\Phi^+\mathbf{r}(\mathbf{u}, t)] + \mathcal{Q}[\Phi^+\mathbf{r}(\mathbf{u}, t)] \equiv \mathbf{r}^{(1)}(\bar{\mathbf{u}}, t) + \mathbf{r}^{(2)}(\mathbf{u}, t) \quad (24)$$

<sup>346</sup> where  $\mathbf{r}^{(1)}(\bar{\mathbf{u}}, t)$  is resolved dynamics that depends on  $\bar{\mathbf{u}}$  only, and  $\mathbf{r}^{(2)}(\mathbf{u}, t)$  is the un-resolved  
<sup>347</sup> or residual dynamics. Detailed derivations and analysis of  $\mathbf{r}^{(1)}(\bar{\mathbf{u}}, t)$  and  $\mathbf{r}^{(2)}(\mathbf{u}, t)$  can be  
<sup>348</sup> found in the Appendix.

<sup>349</sup> It follows from our previous work in Ref. [18] that the resolved dynamics is exactly the  
<sup>350</sup> LCM, where the advection term reduces to zero, i.e.,  $\bar{\mathbf{C}}(\bar{\mathbf{u}}) = \mathbf{0}$ , as shown in the Appendix.  
<sup>351</sup> Using the notation from Eq. (11), it follows that,

$$\begin{aligned}\mathbf{r}^{(1)}(\bar{\mathbf{u}}, t) &= \bar{\mathbf{A}}(\mathbf{w})^{-1}\bar{\mathbf{B}}(\mathbf{w})\bar{\mathbf{u}} + \bar{\mathbf{A}}(\mathbf{w})^{-1}\bar{\mathbf{C}}(\bar{\mathbf{u}})\bar{\mathbf{u}} + \bar{\mathbf{A}}(\mathbf{w})^{-1}\bar{\mathbf{f}}(\bar{\mathbf{u}}) \\ &= \bar{\mathbf{A}}(\mathbf{w})^{-1}\bar{\mathbf{B}}(\mathbf{w})\bar{\mathbf{u}} + \bar{\mathbf{A}}(\mathbf{w})^{-1}\bar{\mathbf{f}}(t)\end{aligned}\quad (25)$$

<sup>352</sup> where the following relations hold,

$$\bar{\mathbf{A}}(\mathbf{w}) = \mathbf{W}(\Phi^+\mathbf{A}^{-1}\Phi)^{-1} \quad (26a)$$

$$\bar{\mathbf{B}}(\mathbf{w}) = \mathbf{W}\Phi^+\mathbf{B}\Phi \quad (26b)$$

<sup>353</sup> where  $\mathbf{W} \in \mathbb{R}^{N \times N}$  is a diagonal matrix with the  $i$ -th element as  $[\mathbf{W}]_{ii} = |\mathcal{V}_k|$  if  $i \in \mathcal{V}_k$ .  
<sup>354</sup> The examination of the second residual term  $\mathbf{r}^{(2)}(\mathbf{u}, t)$  in Eq. (24) is shown in the Appendix,  
<sup>355</sup> and demonstrates that the physical sources of missing dynamics in the LCM include: the  
<sup>356</sup> approximation of non-uniform temperature within each component as a constant, and the  
<sup>357</sup> elimination of the advection term due to coarse-graining. In sum, the above along with the  
<sup>358</sup> derivations in the Appendix not only show that the LCM is a result of coarse-graining of  
<sup>359</sup> the full-order DG-FEM, but also reveal the discrepancies between the LCM and the DG-  
<sup>360</sup> FEM. These discrepancies propagate into the SRM, which as a result of the averaging in the  
<sup>361</sup> LCM formulation, under-predicts the surface recession rates. In the subsequent section, the  
<sup>362</sup> discrepancies in the LCM are corrected to formulate the PIROM.

363 **3.2 Physics-Infusion Via Mori-Zwanzig Formalism**

364 The Mori-Zwanzig (MZ) formalism is an operator-projection technique used to derive ROMs  
 365 for high-dimensional dynamical systems, especially in statistical mechanics and fluid dy-  
 366 namics [13, 14, 15]. It provides an exact reformulation of a high-dimensional Markovian dy-  
 367 namical system, into a low-dimensional observable non-Markovian dynamical system. The  
 368 proposed ROM is subsequently developed based on the approximation to the non-Markovian  
 369 term in the observable dynamics. Particularly, Eq. (24) shows that the DG-FEM dyna-  
 370 mics can be decomposed into the resolved dynamics  $\mathbf{r}^{(1)}(\bar{\mathbf{u}}, t)$  and the orthogonal dynamics  
 371  $\mathbf{r}^{(2)}(\mathbf{u}, t)$ , in the sense of  $\mathcal{P}\mathbf{r}^{(2)} = 0$ . In this case, the MZ formalism can be invoked to ex-  
 372 press the dynamics  $\dot{\bar{\mathbf{u}}}$  in terms of  $\bar{\mathbf{u}}$  alone as the projected Generalized Langevin Equation  
 373 (GLE) [13, 14, 15],

$$\dot{\bar{\mathbf{u}}}(t) = \mathbf{r}^{(1)}(\bar{\mathbf{u}}, t) + \int_0^t \tilde{\kappa}(t, s, \bar{\mathbf{u}}) ds \quad (27)$$

374 where the first and second terms are referred to as the Markovian and non-Markovian terms,  
 375 respectively. The non-Markovian term accounts for the effects of past un-resolved states on  
 376 the current resolved states via a memory kernel  $\tilde{\kappa}(t, s, \bar{\mathbf{u}})$ , which in practice is computa-  
 377 tionally expensive to evaluate.

378 **3.2.1 Markovian Reformulation**

379 This section details the formal derivation of the PIROM as a system of ODEs for the thermal  
 380 dynamics, based on approximations to the memory kernel. Specifically, the kernel  $\tilde{\kappa}$  is  
 381 examined via a leading-order expansion, based on prior work [20]; this can be viewed as an  
 382 analog of zeroth-order holding in linear system theory with a sufficiently small time step. In  
 383 this case, the memory kernel is approximated as,

$$\tilde{\kappa}(t, s, \bar{\mathbf{u}}) \approx \mathbf{r}^{(1)}(\bar{\mathbf{u}}, t) \cdot \nabla_{\bar{\mathbf{u}}} \mathbf{r}^{(2)}(\Phi \bar{\mathbf{u}}, t) \quad (28)$$

384 Note that the terms in  $\mathbf{r}^{(1)}$  have a common factor  $\bar{\mathbf{A}}^{-1}$ ; this motivates the following heuristic  
 385 modification of the model form in Eq. (27),

$$\dot{\bar{\mathbf{u}}} = \mathbf{r}^{(1)}(\bar{\mathbf{u}}, t) + \bar{\mathbf{A}}(\mathbf{w})^{-1} \int_0^t \kappa(t, s, \bar{\mathbf{u}}) ds \quad (29a)$$

$$\bar{\mathbf{A}}(\mathbf{w}) \dot{\bar{\mathbf{u}}} = \bar{\mathbf{B}}(\mathbf{w}) \bar{\mathbf{u}} + \bar{\mathbf{f}}(t) + \int_0^t \kappa(t, s, \bar{\mathbf{u}}) ds \quad (29b)$$

386 where the original kernel  $\tilde{\kappa}$  is effectively normalized by  $\bar{\mathbf{A}}(\mathbf{w})^{-1}$ . Intuitively, such choice  
 387 of kernel reduces its dependency on the averaged material properties, and simplifies the  
 388 subsequent design of model form.

389 Subsequently, the hidden states are introduced to “Markovianize” the system Eq. (27).  
 390 In this manner, Eq. (29b) is converted into a pure state-space model, with the functional  
 391 form of the LCM retained; since LCM is a physics-based model, then it encodes the phys-  
 392 ical information and retains explicit parametric dependence of the problem. Consider the

<sup>393</sup> representation of the kernel as a finite sum of simpler functions, e.g., exponentials,

$$\boldsymbol{\kappa}(t, s, \bar{\mathbf{u}}) = \sum_{j=1}^m \mathcal{K}_j(t, s, \bar{\mathbf{u}}) [\mathbf{p}_j + \mathbf{d}_j(\bar{\mathbf{u}})] \phi_j(s, \bar{\mathbf{u}}) \quad (30)$$

<sup>394</sup> where,

$$\mathcal{K}_j(t, s, \bar{\mathbf{u}}) = e^{-\int_s^t (\lambda_j + e_j(\bar{\mathbf{u}})) d\tau}, \quad \phi_j(s, \bar{\mathbf{u}}) = \mathbf{q}_j^\top \bar{\mathbf{u}}(s) + \mathbf{g}_j(\bar{\mathbf{u}})^\top \bar{\mathbf{u}}(s) + \mathbf{r}_j^\top \bar{\mathbf{f}}(s) \quad (31)$$

<sup>395</sup> with suitable coefficients  $\mathbf{p}_j, \mathbf{d}_j, \mathbf{q}_j, \mathbf{g}_j, \mathbf{r}_j \in \mathbb{R}^N$  and decay rates  $\lambda_j, e_j(\bar{\mathbf{u}}) > 0$ , that need to  
<sup>396</sup> be identified from data.

<sup>397</sup> Define the hidden states as,

$$\beta_j(t) = \int_0^t \mathcal{K}_j(s, \bar{\mathbf{u}}) \phi_j(s, \bar{\mathbf{u}}) ds \quad (32)$$

<sup>398</sup> and differentiate with respect to time,,

$$\dot{\beta}_j(t) = -[\lambda_j + e_j(\bar{\mathbf{u}})] \beta_j(t) + \mathbf{q}_j^\top \bar{\mathbf{u}}(t) + \mathbf{g}_j(\bar{\mathbf{u}})^\top \bar{\mathbf{u}}(t) + \mathbf{r}_j^\top \bar{\mathbf{f}}(t) \quad (33)$$

<sup>399</sup> to obtain the memory,

$$\int_0^t \boldsymbol{\kappa}(t, s, \bar{\mathbf{u}}) ds = \sum_{j=1}^m [\mathbf{p}_j + \mathbf{d}_j(\bar{\mathbf{u}})] \beta_j(t) \quad (34)$$

<sup>400</sup> Then, Eq. (29b) is recast as the extended Markovian system,

$$\bar{\mathbf{A}}(\mathbf{w}) \dot{\bar{\mathbf{u}}} = \bar{\mathbf{B}}(\mathbf{w}) \bar{\mathbf{u}} + [\mathbf{P} + \mathbf{D}(\bar{\mathbf{u}})] \boldsymbol{\beta} + \bar{\mathbf{f}}(t) \quad (35a)$$

$$\dot{\boldsymbol{\beta}} = [\mathbf{Q} + \mathbf{G}(\bar{\mathbf{u}})] \bar{\mathbf{u}} + [\mathbf{E}(\bar{\mathbf{u}}) - \boldsymbol{\Lambda}] \boldsymbol{\beta} + \mathbf{R} \bar{\mathbf{f}}(t) \quad (35b)$$

<sup>401</sup> where the data-driven operators associated to the hidden dynamics are collected as,

$$\boldsymbol{\Lambda} = \text{diag}[\lambda_1, \lambda_2, \dots, \lambda_m] \in \mathbb{R}^{m \times m}, \quad \mathbf{P} = [\mathbf{p}_1, \mathbf{p}_2, \dots, \mathbf{p}_m] \in \mathbb{R}^{N \times m} \quad (36a)$$

$$\mathbf{D}(\bar{\mathbf{u}}) = [\mathbf{d}_1(\bar{\mathbf{u}}), \mathbf{d}_2(\bar{\mathbf{u}}), \dots, \mathbf{d}_m(\bar{\mathbf{u}})] \in \mathbb{R}^{N \times m}, \quad \mathbf{Q} = [\mathbf{q}_1, \mathbf{q}_2, \dots, \mathbf{q}_m] \in \mathbb{R}^{m \times N} \quad (36b)$$

$$\mathbf{G}(\bar{\mathbf{u}}) = [\mathbf{g}_1(\bar{\mathbf{u}}), \mathbf{g}_2(\bar{\mathbf{u}}), \dots, \mathbf{g}_m(\bar{\mathbf{u}})] \in \mathbb{R}^{m \times N}, \quad \mathbf{R} = [\mathbf{r}_1, \mathbf{r}_2, \dots, \mathbf{r}_m] \in \mathbb{R}^{m \times N} \quad (36c)$$

$$\mathbf{E}(\bar{\mathbf{u}}) = \text{diag}[e_1(\bar{\mathbf{u}}), e_2(\bar{\mathbf{u}}), \dots, e_m(\bar{\mathbf{u}})] \in \mathbb{R}^{m \times m} \quad (36d)$$

<sup>402</sup> The form of the temperature-dependent matrices  $\mathbf{D}(\bar{\mathbf{u}})$ ,  $\mathbf{G}(\bar{\mathbf{u}})$ , and  $\mathbf{E}(\bar{\mathbf{u}})$  is specified in the  
<sup>403</sup> next section. Since the hidden states  $\boldsymbol{\beta}$  serve as the memory, their initial conditions are set  
<sup>404</sup> to zero, i.e.,  $\boldsymbol{\beta}(t_0) = \mathbf{0}$ , no memory at the beginning. The physics-infused model in Eq. (35)  
<sup>405</sup> retains the structure of the LCM and depend on the displacements  $\mathbf{w}$ , while the hidden states  
<sup>406</sup> account for missing physics through corrections to the stiffness and advection matrices, as  
<sup>407</sup> well as the forcing term.

408 **3.2.2 Coupled Physics-Infused Model**

409 The next step involves coupling the physics-infused model in Eq. (35) with the SRM in  
 410 Eq. (10) to define the PIROM for ablating TPS. To this end, define the surface temperature  
 411  $\mathbf{z}_u \in \mathbb{R}^{\tilde{N}}$  and displacements  $\mathbf{z}_w \in \mathbb{R}^{\tilde{N}}$  for  $\tilde{N} \leq N$  ablating components so that the observable  
 412 is given by  $\mathbf{z} = [\mathbf{z}_u, \mathbf{z}_w]^\top \in \mathbb{R}^{n_z}$  with  $n_z = 2\tilde{N}$  as the total number of observables.

413 Collect the RPM and hidden states into a single state vector  $\mathbf{y} = [\bar{\mathbf{u}}, \mathbf{w}, \boldsymbol{\beta}]^\top \in \mathbb{R}^{n_y}$ , where  
 414  $n_y = N + \tilde{N} + m$ , and define a data-driven operator  $\mathbf{M} \in \mathbb{R}^{n_z \times n_y}$  to define the PIROM's  
 415 observable as,

$$\mathbf{z} = \mathbf{My} \quad (37)$$

416 where,

$$\mathbf{M} = \begin{bmatrix} \mathbf{M}_{\bar{u}} & \mathbf{0} & \mathbf{M}_{\boldsymbol{\beta}} \\ \mathbf{0} & \mathbf{I} & \mathbf{0} \end{bmatrix} \quad (38)$$

417 includes the matrices  $\mathbf{M}_{\bar{u}} \in \mathbb{R}^{\tilde{N} \times N}$  and  $\mathbf{M}_{\boldsymbol{\beta}} \in \mathbb{R}^{\tilde{N} \times m}$ , which computes the surface tem-  
 418 perature observable from the RPM states and hidden states, respectively. The PIROM is  
 419 coupled to the SRM in Eq. (10) by leveraging Eq. (37) to compute the surface recession  
 420 velocity. Thus, the PIROM is formally stated as,

$$\mathcal{A}\dot{\mathbf{y}} = [\mathcal{B} + \mathcal{C}]\mathbf{y} + \mathcal{F}(t) \quad (39a)$$

$$\mathbf{z} = \mathbf{My} \quad (39b)$$

421 where,

$$\mathcal{A} = \begin{bmatrix} \bar{\mathbf{A}}(\mathbf{w}) & \mathbf{O} & \mathbf{O} \\ \mathbf{O} & \mathbf{I} & \mathbf{O} \\ \mathbf{O} & \mathbf{O} & \mathbf{I} \end{bmatrix} \in \mathbb{R}^{n_y \times n_y}, \quad \mathcal{B} = \begin{bmatrix} \bar{\mathbf{B}}(\mathbf{w}) & \mathbf{O} & \mathbf{P} \\ \Xi\mathbf{M}_u & \mathbf{O} & \Xi\mathbf{M}_{\boldsymbol{\beta}} \\ \mathbf{Q} & \mathbf{O} & -\Lambda \end{bmatrix} \in \mathbb{R}^{n_y \times n_y}, \quad (40a)$$

$$\mathcal{C} = \begin{bmatrix} \mathbf{O} & \mathbf{O} & \mathbf{D}(\bar{\mathbf{u}}) \\ \mathbf{O} & \mathbf{O} & \mathbf{O} \\ \mathbf{G}(\bar{\mathbf{u}}) & \mathbf{O} & \mathbf{E}(\bar{\mathbf{u}}) \end{bmatrix} \in \mathbb{R}^{n_y \times n_y}, \quad \mathcal{F} = \begin{bmatrix} \bar{\mathbf{f}}(t) \\ -\bar{\mathbf{f}} \\ \mathbf{R}\bar{\mathbf{f}}(t) \end{bmatrix} \in \mathbb{R}^{n_y} \quad (40b)$$

422 The learnable parameters in the PIROM are collected as,

$$\Theta = \{\mathbf{P}, \Lambda, \mathbf{Q}, \mathbf{M}, \mathbf{D}(\bar{\mathbf{u}}), \mathbf{G}(\bar{\mathbf{u}}), \mathbf{E}(\bar{\mathbf{u}}), \mathbf{R}\}, \in \mathbb{R}^{n_\theta} \quad (41)$$

423 The matrices  $\mathbf{P}, \Lambda, \mathbf{Q}, \mathbf{M}, \mathbf{R}$  are constants, and account for the effects of coarse-graining on  
 424 the stiffness, output, and forcing matrices. The matrices  $\mathbf{D}(\bar{\mathbf{u}}), \mathbf{E}(\bar{\mathbf{u}}), \mathbf{G}(\bar{\mathbf{u}})$  are temperature-  
 425 dependent matrices, and account for the effects of coarse-graining on the advection matrix  
 426 due to mesh motion. Leveraging the DG-FEM formula for the advection matrix in Eq. (56c)  
 427 in the Appendix, and noting that the ablating velocity in Eq. (4) imposes the boundary  
 428 condition for the mesh motion, the state-dependent matrices for the  $i$ -th component are  
 429 written as,

$$\mathbf{D}(\bar{\mathbf{u}}) \approx \text{diag}[\dot{\mathbf{w}}] \mathbf{D}, \quad \mathbf{G}(\bar{\mathbf{u}}) \approx \mathbf{G} \text{diag}[\dot{\mathbf{w}}], \quad \mathbf{E}(\bar{\mathbf{u}}) \approx \text{diag} \left[ \underbrace{\dot{\mathbf{w}}, \dots, \dot{\mathbf{w}}}_{\tilde{m} \text{ times}} \right] \mathbf{E} \quad (42)$$

430 where  $\dot{\mathbf{w}} = \dot{\mathbf{w}}(\bar{\mathbf{u}})$  is the SRM based on the observable temperature  $\bar{\mathbf{u}}$  and  $\tilde{m}$  is the number  
 431 of hidden states per component so that  $m = N\tilde{m}$ .

432 The PIROM in Eq. (39) incorporates explicit information on the material properties,  
 433 boundary conditions, and surface recession, and is designed to generalize across parametric  
 434 variations in these inputs. Moreover, the hidden dynamics in Eq. (35) are interpretable, as  
 435 these retain the functional form of the DG-FEM in Eq. (7). The next step is focused on  
 436 identifying the unknown data-driven parameters  $\Theta$  characterizing the hidden dynamics.

### 437 3.3 Learning the Hidden Dynamics

438 Learning of the PIROM is achieved through a gradient-based neural-ODE-like approach [3].  
 439 For ease of presentation, consider the compact form of the PIROM in Eq. (39),

$$440 \quad \mathcal{D}(\dot{\mathbf{y}}, \mathbf{y}, \boldsymbol{\xi}, \mathcal{F}; \Theta) = \mathbf{0} \quad (43)$$

440 where  $\boldsymbol{\xi}$  defines the model parameters, i.e., SRM parameters, while  $\mathcal{F}$  represents the forcing  
 441 terms, i.e., the boundary conditions.

442 Consider a dataset of  $N_s$  high-fidelity *surface temperature* observable trajectories  $\mathbf{z}_{\text{HF}}$ ,  
 443 sampled at  $p$  time instances  $\{t_k\}_{k=0}^{p-1}$ , for different parameter settings  $\{\boldsymbol{\xi}^{(l)}\}_{l=1}^{N_s}$  and forcing  
 444 functions  $\{\mathcal{F}^{(l)}(t)\}_{l=1}^{N_s}$ . The dataset is expressed as,

$$445 \quad \mathcal{D} = \left\{ \left( t_k, \mathbf{z}_{\text{HF}}^{(l)}(t_k), \boldsymbol{\xi}^{(l)}, \mathcal{F}^{(l)}(t_k) \right) \right\}_{l=1}^{N_s}, \quad k = 0, 1, \dots, p-1 \quad (44)$$

445 In this work, the dataset contains only surface temperature observables – all high-fidelity  
 446 information regarding the surface displacements *are assumed to be unavailable during learning*.  
 447

448 The learning problem is formulated as the following differentially-constrained problem,

$$449 \quad \min_{\Theta} \quad \mathcal{J}(\Theta; \mathcal{D}) = \sum_{l=1}^{N_s} \int_{t_0}^{t_f} \ell \left( \mathbf{z}_u^{(l)}, \mathbf{z}_{\text{HF}}^{(l)} \right) dt \quad (45a)$$

$$450 \quad \text{s.t.} \quad \mathbf{0} = \mathcal{D} \left( \dot{\mathbf{y}}^{(l)}, \mathbf{y}^{(l)}, \boldsymbol{\xi}^{(l)}, \mathcal{F}^{(l)}; \Theta \right) \quad (45b)$$

451 for  $l = 1, 2, \dots, N_s$ , the objective is to minimize the discrepancy between the high-fidelity  
 452 and PIROM predictions for the  $l$ -th trajectory with  $\ell \left( \mathbf{z}_u^{(l)}, \mathbf{z}_{\text{HF}}^{(l)} \right) = \left\| \mathbf{z}_u^{(l)} - \mathbf{z}_{\text{HF}}^{(l)} \right\|_2^2$ .

453 The gradient-based optimization loop is based on the adjoint variable  $\boldsymbol{\lambda}$ , governed by the  
 454 adjoint differential equation,

$$455 \quad \frac{\partial \ell}{\partial \mathbf{y}} + \boldsymbol{\lambda}^\top \frac{\partial \mathcal{D}}{\partial \mathbf{y}} - \frac{d}{dt} \left( \boldsymbol{\lambda}^\top \frac{\partial \mathcal{D}}{\partial \dot{\mathbf{y}}} \right) = \mathbf{0} \quad (46a)$$

$$456 \quad \boldsymbol{\lambda}(t_f)^\top \frac{\partial \mathcal{D}}{\partial \dot{\mathbf{y}}(t_f)} = \mathbf{0} \quad (46b)$$

453 Once  $\boldsymbol{\lambda}$  is solved, the gradient is computed as,

$$\nabla_{\Theta} \mathcal{J} = \frac{1}{N_s} \sum_{l=1}^{N_s} \int_{t_0}^{t_f} \left( \frac{\partial \ell}{\partial \Theta} + (\boldsymbol{\lambda}^{(l)})^\top \frac{\partial \mathcal{D}}{\partial \Theta} \right) dt \quad (47)$$

454 The PIROM parameters  $\Theta$  are updated via stochastic gradient descent using ML optimizers  
455 such as Adam. The learning procedure iterates between solving the PIROM in Eq. (43)  
456 forward in time, solving the adjoint equation in Eq. (46) backward in time, and updating  
457 the parameters  $\Theta$  until convergence.

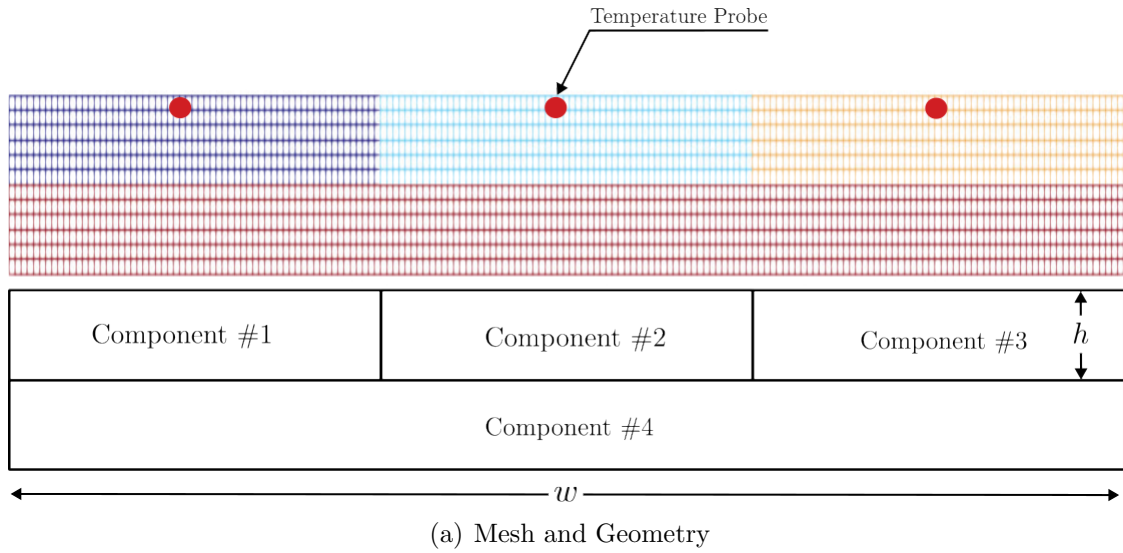
## 458 4 Application to Thermal Protection Systems

459 In this section, the proposed PIROM approach is applied to the analysis of thermo-ablative  
460 multi-layered hypersonic TPS. The performance of the PIROM is evaluated in terms of the  
461 three corners of the ITM in Fig. 1, based on parametric variations of boundary conditions and  
462 SRMs. The results show PIROM to be a promising candidate for the solution of the impos-  
463 sible trinity of modeling, achieving RPM-level computational efficiency and generalizability,  
464 while attaining high-fidelity model accuracy.

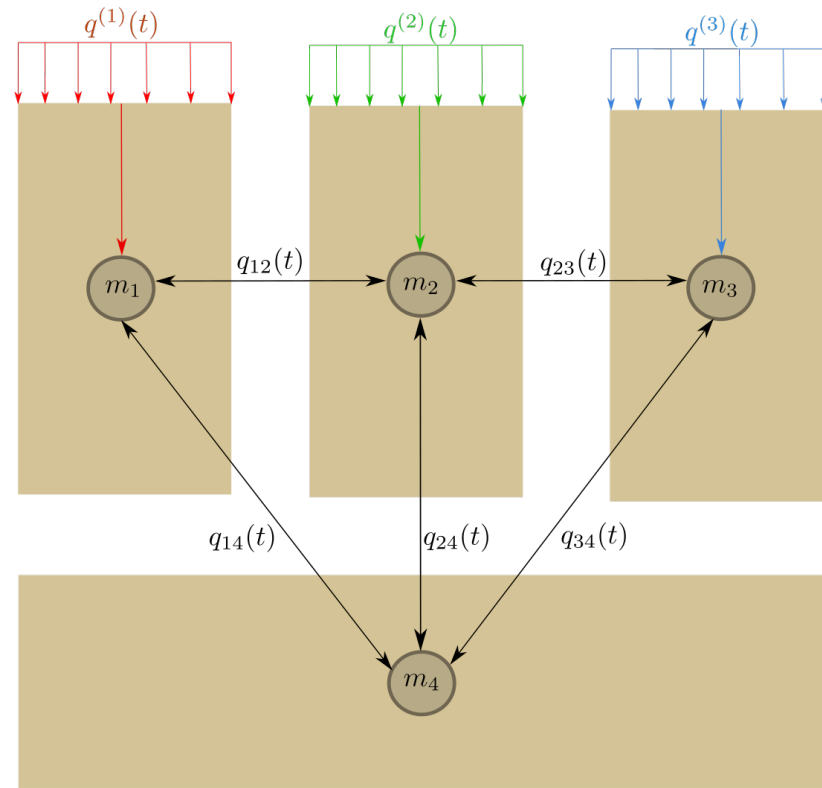
### 465 4.1 Problem Definition

466 Consider the two-dimensional TPS configuration shown in Fig. 3 with constant material  
467 properties within each layer, dimensions, and BCs listed in Table 1. Such configuration is  
468 representative of the TPS used for the initial concept 3.X vehicle in past studies [10], and in-  
469 volves two main layers: an outer ablative layer, and an inner substrate layer. The top ablative  
470 layer may be composed of different materials, such as PICA or Avcoat, while the substrate  
471 layer is typically made of a high-temperature resistant material, such as carbon-carbon com-  
472 posite [7]. The ablative layer, composed of  $\tilde{N} = 3$  ablative components, is subjected to  
473 strong time-varying and non-uniform heating, while the substrate layer, composed of one  
474 non-ablative component, is insulated adiabatically at the outer surface; the total number of  
475 components is thus  $N = 4$ .

476 The lumped-mass representation of the TPS configuration is shown in Fig. 3(b), where  
477 each component  $\Omega_i$  is represented by a lumped mass with uniform temperature  $\bar{u}_i(t)$ . Details  
478 regarding the derivation of the LCM for this configuration are provided in Appendix A.  
479 The sources of non-linearities studied in this problem originate from the coupling between  
480 the thermodynamics and temperature-dependent mesh motion, i.e., geometry-dependent  
481 matrices and temperature advection, as well as the heterogeneities across material layers.  
482 As shown in Fig. 3, perfect thermocouple devices are placed at the surfaces of the ablative  
483 layers for the collection of the high-fidelity temperature signals that are used in the following  
484 sections for training and testing the PIROM.



(a) Mesh and Geometry



(b) Lumped Mass Representation

Figure 3: Four-component TPS geometry and lumped-mass representation for the TPS.

Component	$w$ (cm)	$h$ (cm)	$\rho$ (kg/m <sup>3</sup> )	$c_p$ (J/kg·K)	$k$ (W/m·K)	$\alpha \times 10^{-6}$ (m/s·K)
#1	0.3	0.03	160	1200	0.2	1
#2	0.3	0.03	1800	900	5	1
#3	0.3	0.03	300	1500	0.15	1
#4	0.9	0.03	1600	800	10	0

Table 1: Description of TPS components, including thickness  $h$ , density  $\rho$ , specific heat capacity  $c_p$ , thermal conductivity  $k$ , and SRM parameter  $\alpha$ .

## 4.2 Problem Parametrization

The operating conditions of the TPS are specified by the boundary conditions, i.e., the heat flux, and the SRM matrix  $\boldsymbol{\Xi}$ . Specifically, the heat flux on the Neumann BC is parametrized using  $\boldsymbol{\xi}_{\text{BC}} = \{\xi_1, \xi_2, \xi_3\}$ , while the SRM is parametrized using  $\boldsymbol{\xi}_{\text{SRM}} = \{\alpha_1, \alpha_2, \alpha_3\}$ . Thus, the heat flux and SRM over the  $i$ -th ablative component are expressed as,

$$q_i(x, t; \boldsymbol{\xi}_{\text{BC}}) = \xi_1 e^{\xi_2 x} e^{\xi_3 t}, \quad \forall x \in \Gamma_{i,q}, \quad \dot{w}_i(z_{u,i}; \boldsymbol{\xi}_{\text{SRM}}) = \alpha_i (z_{u,i} - u_{0,i}), \quad i = 1, \dots, \tilde{N} \quad (48)$$

where  $\Gamma_{i,q}$ ,  $z_{u,i}$ , and  $u_{0,i}$  correspond to the Neumann BC surface, the surface temperature prediction, and the initial temperature of the  $i$ -th ablative component, respectively. The parameters  $\xi_1$ ,  $\xi_2$ , and  $\xi_3$  control the heat flux magnitude, spatial variation, and temporal variation, respectively. The constant  $\alpha_i$  is a small material-dependent constant determined from the B' table [12], specifying the surface recession velocity for a given temperature.

## 4.3 Data Generation

Full-order solutions of the TPS are computed using the FEM multi-mechanics module from the **Aria** package with the mesh shown in Fig. 3(a) [4]. The mesh consists of 2196 total elements, with 366 elements for each ablative component and 1098 elements for the substrate component. Given an operating condition  $\boldsymbol{\xi} = [\boldsymbol{\xi}_{\text{BC}}, \boldsymbol{\xi}_{\text{SRM}}]^\top$ , a high-fidelity solution is computed for one minute, starting from an uniform initial temperature of  $T(x, t_0) = 300$  K. Each solution consist of a collection of space-time-varying temperature and displacement fields  $\left\{ \left( t_k, \mathbf{u}_{\text{HF}}^{(l)}(t_k), \mathbf{d}_{\text{HF}}^{(l)}(t_k), \boldsymbol{\xi}^{(l)} \right) \right\}_{k=0}^{p-1}$ , where  $p$  is the number of time steps with a step size of  $\Delta t \approx 10^{-3}$ . The observable trajectories are representative of near-wall thermocouple sensing of hypersonic flows involving heat transfer. At each time instance  $t_k$ , a temperature reading is recorded from each ablative component using the thermocouples shown in Fig. 3, resulting in three temperature signals, i.e., the observables  $\mathbf{z}_{\text{HF}} \in \mathbb{R}^3$ . Therefore, each full-order solution produces one trajectory of observables  $\left\{ \left( t_k, \mathbf{z}_{\text{HF}}^{(l)}(t_k), \boldsymbol{\xi}^{(l)} \right) \right\}_{k=0}^{p-1}$ . The goal of the PIROM is to predict the surface temperature and displacement as accurately as possible.

### 4.3.1 Definition of Training and Testing Datasets

The range of parameters used to generate the training  $\mathcal{D}_1$  and testing  $\{\mathcal{D}_2, \mathcal{D}_3\}$  datasets are listed in Table 2. The training and testing datasets are designed, respectively, to: (1)

Dataset	Parameters					
	$\xi_1 \times 10^3$	$\xi_2 \times 10^{-1}$	$\xi_3 \times 10^{-2}$	$\alpha_1 \times 10^{-6}$	$\alpha_2 \times 10^{-6}$	$\alpha_3 \times 10^{-6}$
$\mathcal{D}_1$	[-6.059, -5.902]	[-3.501, 3.152]	[9.670, 10.464]	1	1	1
$\mathcal{D}_2$	[-6.122, -5.887]	[-3.601, -3.074]	[9.218, 11.246]	1	1	1
$\mathcal{D}_3$	6	-3.333	10	[0.6, 1.5]	[0.6, 1.5]	[0.6, 1.5]

Table 2: Range of parameters [min, max] in training and testing datasets.

512 minimize the information that the PIROM can “see”, and (2) to maximize the variability  
 513 of test operating conditions to examine the PIROM’s generalization performance. A  
 514 total of 110 normally-distributed data points for the BC parametrization are visualized in  
 515 Fig. 4(a), and the corresponding observable trajectories are shown in Figs. 4(b) and 4(c).  
 516 The training dataset  $\mathcal{D}_1$  includes 10 trajectories with randomly selected BC parameters from  
 517 the 110 points, with nominal SRM parameters  $\boldsymbol{\xi}_{\text{SRM}} = \{1, 1, 1\} \times 10^{-6}$ . Note that although  
 518 Fig. 4(c) shows the surface displacements for all ablative components in  $\mathcal{D}_1$ , only the *surface*  
 519 *temperature is used for training the PIROM.*

520 Two additional datasets are generated for testing. The dataset  $\mathcal{D}_2$  includes the remaining  
 521 100 BC parameter values not considered in  $\mathcal{D}_1$ , and the high-fidelity simulation are generated  
 522 with the same nominal SRM parameters. The cases in the  $\mathcal{D}_3$  fixes the boundary condition  
 523 as shown in Fig. 4(a) and varies the SRM parameters as shown in Table. 2. The testing  
 524 datasets  $\mathcal{D}_2$  and  $\mathcal{D}_3$  are *out-of-distribution* (OOD) datasets, and are meant for testing the  
 525 generalizability of the ROMs to unseen BCs and SRMs, respectively.

#### 526 4.4 Performance Metrics

527 The performance metrics are defined to quantitatively assess the solution to the ITM for the  
 528 TPS problem. Specifically, the *accuracy* metric quantifies the prediction error of the ROMs  
 529 against high-fidelity solutions. The *efficiency* metric quantifies the computational speedup  
 530 achieved by the ROMs compared to high-fidelity simulations. The *generalizability* metric  
 531 quantifies the ability of the ROMs to retain accuracy when evaluated on OOD datasets.  
 532 Together, these metrics provide a comprehensive evaluation of the PIROM’s performance  
 533 in addressing the challenges associated with modeling complex multi-physics systems. Since  
 534 the generalizability metric is inherently tied to the accuracy metric when evaluated on OOD  
 535 datasets, the following sections focus on defining the accuracy and efficiency metrics.

536 **Accuracy Metric** Consider one trajectory of high-fidelity surface temperature and dis-  
 537 placement data  $\left\{ \left( t_k, \mathbf{z}_{u,\text{HF}}^{(l)}(t_k), \mathbf{z}_{w,\text{HF}}^{(l)}(t_k) \right) \right\}_{k=0}^{p-1}$  for the  $l$ -th operating condition in the testing  
 538 datasets  $\mathcal{D}_2$  or  $\mathcal{D}_3$ . The difference  $e_i^{(l)}$  for the  $i$ -th predicted observable, denoted as  $z_i^{(l)}$ , is  
 539 computed as,

$$e_i^{(l)} = \frac{1}{\Delta z_i^{(l)}} \sqrt{\frac{1}{p} \sum_{k=0}^{p-1} \left( z_{i,\text{HF}}^{(l)}(t_k) - z_i^{(l)}(t_k) \right)^2} \quad (49)$$

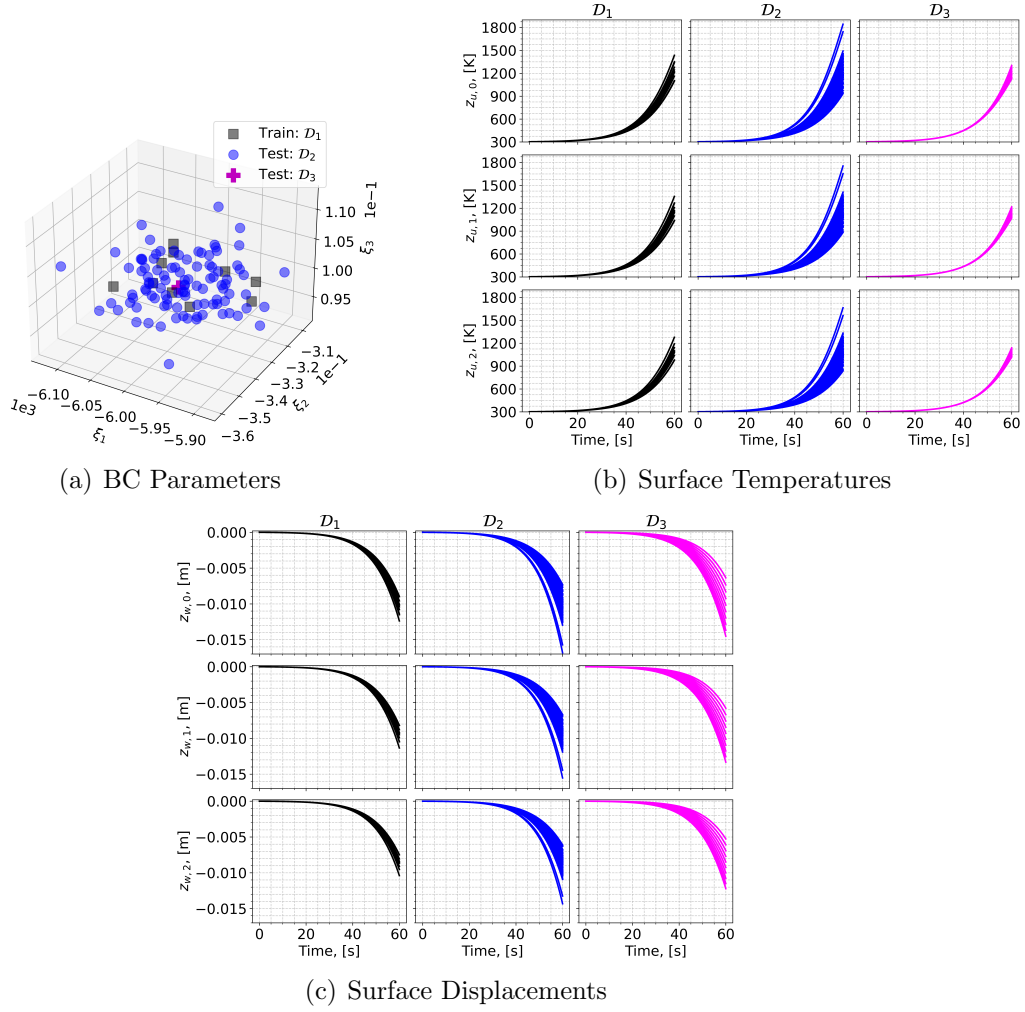


Figure 4: Boundary condition parameters, temperature observables, and displacement observables for the training and testing datasets. The variables  $z_{u,i}$  and  $z_{w,i}$  correspond to the surface temperature and displacement of the  $i$ -th ablative component, respectively.

540 for  $i = 1, 2, 3$  and  $z_i^{(l)} \in \{z_{i,u}^{(l)}, z_{i,w}^{(l)}\}$ , and where,

$$\Delta z_i^{(l)} = \max_{0 \leq k \leq p-1} z_{i,\text{HF}}^{(l)}(t_k) - \min_{0 \leq k \leq p-1} z_{i,\text{HF}}^{(l)}(t_k) \quad (50)$$

541 Subsequently, the prediction error of one trajectory is computed by a weighted sum based  
 542 on the area of each *ablative component*, resulting in the normalized root mean square error  
 543 (NRMSE) metric for one trajectory,

$$\text{NRMSE} = \frac{\sum_{i=1}^{\tilde{N}} |\Omega_i| e_i^{(l)}}{\sum_{i=1}^{\tilde{N}} |\Omega_i|} \times 100\% \quad (51)$$

544 For one dataset, the NRMSE is defined to be the average of the NRMSEs of all trajectories  
 545 in the dataset.

546 **Efficiency Metric** The efficiency metric is quantified using the *computational acceleration*,  
 547 which focuses on the quantification of the spedup factor  $\frac{\mathcal{T}_{\text{HF}}(\mathcal{D})}{\mathcal{T}_{\mathcal{M}}(\mathcal{D})}$ . The terms  $\mathcal{T}_{\text{HF}}(\mathcal{D})$  and  
 548  $\mathcal{T}_{\mathcal{M}}(\mathcal{D})$  correspond to the wall-clock time required by the high-fidelity model and the ROM,  
 549 to evaluate all trajectories in the dataset  $\mathcal{D}$ , respectively. Here,  $\mathcal{M}$  corresponds to the ROM  
 550 under consideration, i.e., either the PIROM or the RPM. For a benchmark analysis of the  
 551 computational costs during the training phase, please refer to Ref. [18].

## 552 4.5 Generalization to Boundary Conditions

553 To assess generalization to BC, the PIROM and RPM are evaluated on the  $\mathcal{D}_2$  dataset.  
 554 Temperature trajectory predictions for a representative test case are shown in Figs. 5(a)  
 555 and 5(b), where the PIROM accurately captures the surface temperature and displacement  
 556 dynamics, while the RPM exhibits larger deviations and under-predicts surface displace-  
 557 ments due to the averaging effects of the LCM. The mean NRMSE across all test cases in  
 558  $\mathcal{D}_2$  is shown in Figs. 5(e) and 5(f), where the PIROM consistently achieves errors of 1% for  
 559 both temperature and displacement predictions, improving the RPM's accuracy by an order  
 560 of magnitude. Figure 5 reports the average substrate temperature, where the LCM remains  
 561 highly accurate due to the symmetric TPS geometry, adiabatic BCs, and negligible thermal  
 562 gradients within the substrate. Although the PIROM is trained only on the surface temper-  
 563 atures of the three ablative components, its hidden dynamics retain the LCM's accuracy for  
 564 this untrained observable, demonstrating the PIROM's ability to generalize and preserve the  
 565 underlying physics of the reduced-physics backbone. The consistent low predictions errors  
 566 demonstrate the solution to the *accuracy* corner of the ITM.

## 567 4.6 Generalization to Surface Recession Models

568 The generalization performance of the PIROM and RPM is also evaluated on surface reces-  
 569 sion models using the OOD  $\mathcal{D}_3$  dataset. As detailed in Table 1, the SRM parameter  $\alpha$  in  $\mathcal{D}_3$   
 570 is perturbed 10 times by up to  $\pm 50\%$  from their nominal values. The SRM model perturba-  
 571 tion introduces significant changes to the ablative layer dynamics, potentially increasing the

572 rate of ablation at lower temperatures, as shown in Figs. 5(c) and 5(d). The PIROM, with-  
573 out considering any SRM variations during training, is able to accurately predict the surface  
574 temperature and displacement dynamics for the perturbed SRMs. Figures 5(e) and 5(f) show  
575 the mean NRMSE across all test cases in  $\mathcal{D}_3$ , where the PIROM consistently achieves errors  
576 below 1% for both temperature and displacement predictions, and consistently improves the  
577 RPM’s accuracy by approximately an order of magnitude. The consistent low prediction  
578 errors demonstrate the solution to the *generalizability* corner of the ITM.

## 579 4.7 Computational Cost

580 All computations are performed in serial for fairness on an Intel Xeon (R) Gold 6258R  
581 CPU 2.70GHz computer with 62 GB of RAM. The numerical integration for the RPM  
582 and PIROM models are performed using SciPy’s `solve_ivp` function with default settings.  
583 Provided a parametrization for the BC and SRM, the high-fidelity FEM simulation takes  
584 about  $\approx 60$  seconds, the RPM takes about  $\approx 0.137$  seconds, and the PIROM takes about  
585  $\approx 0.280$  seconds. Therefore, during evaluation both the RPM and PIROM achieve speedup  
586 factors of approximately 438 and 214, respectively, over the high-fidelity model. As a result,  
587 the PIROM and RPM are *two-orders-of-magnitude faster* than the high-fidelity model. The  
588 PIROM nearly preserves the computational efficiency of the RPM (about twice as expensive  
589 as the RPM), while achieving significantly higher accuracy and generalization capabilities.  
590 The results demonstrate the benefits of physics-infused modeling for the development of  
591 efficient and generalizable ROMs for complex multi-physics systems, and demonstrate the  
592 solution to the *efficiency* corner of the ITM.

## 593 4.8 Summary of Results

594 The results presented in this section demonstrate the accuracy, generalizability, and com-  
595 putational efficiency of the proposed PIROM approach for the analysis of thermo-ablative  
596 multi-layered hypersonic TPS. The PIROM consistently achieves low prediction errors below  
597 1% for both surface temperature and displacement across a range of unseen boundary con-  
598 ditions and surface recession models. Furthermore, the PIROM retains the computational  
599 efficiency of traditional RPMs, achieving speedup factors of over 200 times compared to high-  
600 fidelity FEM simulations. The generalization capabilities of the PIROM are attributed to its  
601 hybrid structure: a physics-based LCM backbone that ensures consistency with the under-  
602 lying thermodynamics, while a data-driven correction mechanism captures the un-resolved  
603 dynamics. For this TPS problem, the PIROM successfully addresses the impossible trinity of  
604 modeling, achieving high-fidelity model accuracy, RPM-level computational efficiency, and  
605 generalizability to unseen operating conditions.

## 606 5 Conclusions

607 This work presents the development and validation of the *scientific machine learning* frame-  
608 work termed *Physics-Informed Reduced Order Model* (PIROM) for simulating the transient

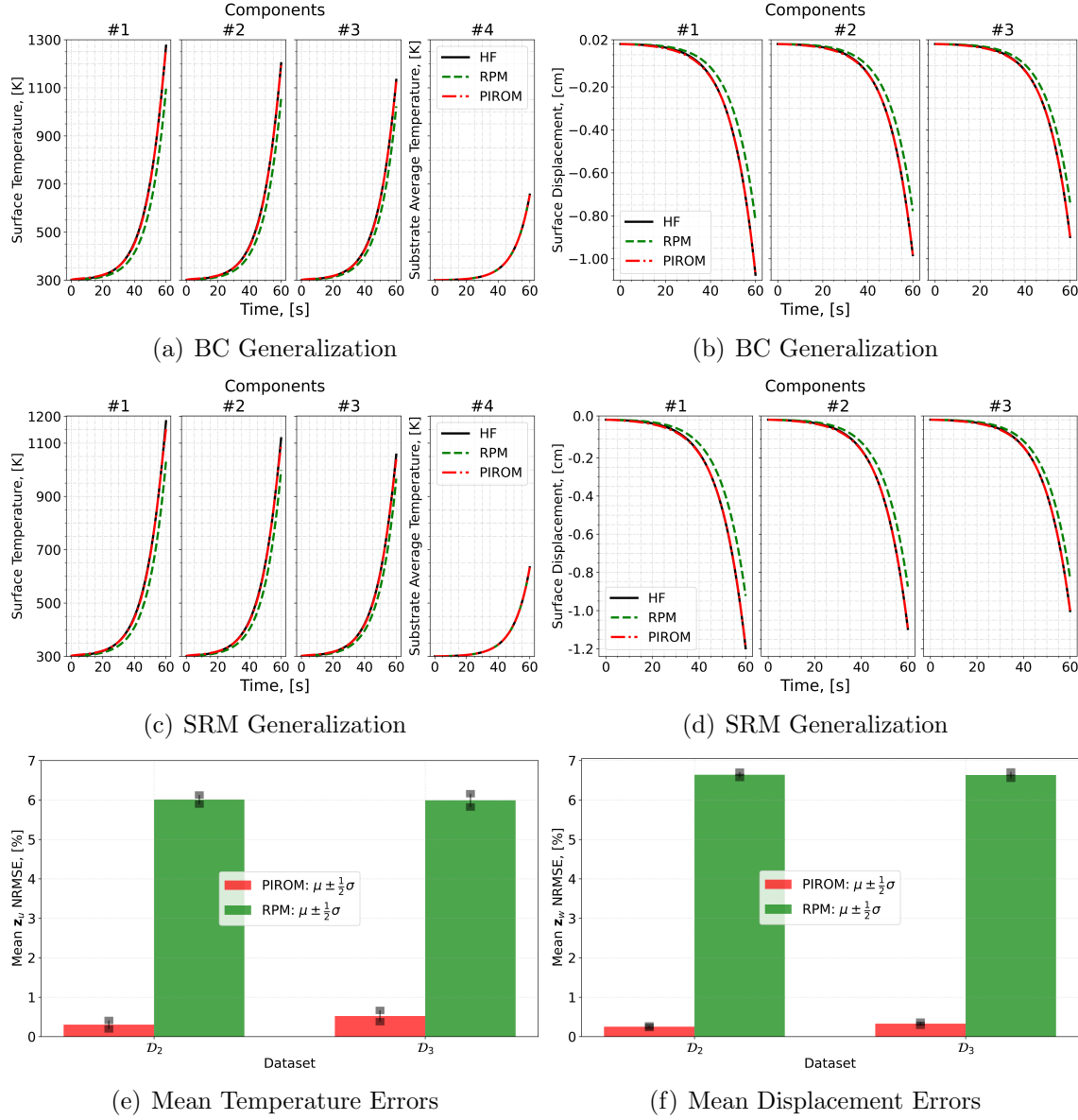


Figure 5: PIROM predictions against high-fidelity solutions for (a)-(b) BC generalization, (c)-(d) SRM generalization, and (e)-(f) mean errors across testing datasets.

609 thermo-ablative response of hypersonic thermal protection systems (TPS) subjected to hy-  
610 personic boundary layers. Using coarse-graining on a DG-FEM model and the Mori-Zwanzig  
611 formalism, the PIROM formulation in Ref. [18] is extended to account for non-decomposing  
612 thermo-ablative response of a multi-layered TPS. The PIROM builds upon the following two  
613 key components: (1) a first-order physics-based model, i.e., the RPM based on LCM and  
614 SRM, for low-fidelity predictions of the surface temperature and recession; and (2) a data-  
615 driven closure to the non-Markovian term in the Generalized Langevin Equation (GLE). The  
616 non-Markovian closure is recast as a set of hidden states that evolve according to a data-  
617 driven dynamical system that is learned from a sparse collection of high-fidelity temperature  
618 signals.

619 The results demonstrate that the PIROM framework effectively reconciles the trade-offs  
620 between accuracy, generalizability, and efficiency of the ITM for simulating ablating hy-  
621 personic TPS. The PIROM consistently achieves mean observable prediction errors of less  
622 than 1% for extrapolative settings involving time-and-space varying boundary conditions  
623 and SRM models. Notably, the PIROM improves the RPM’s accuracy by an order of magni-  
624 tude while preserving its computational efficiency, physical interpretability, and parametric  
625 generalizability. Moreover, the PIROM delivers online evaluations that are two orders of  
626 magnitude faster than the FOM. These results highlight the PIROM’s potential as a promis-  
627 ing framework for optimizing multi-physical dynamical systems, such as TPS under diverse  
628 operating conditions.

## 629 Acknowledgments

630 Sandia National Laboratories is a multimission laboratory managed and operated by Na-  
631 tional Technology & Engineering Solutions of Sandia, LLC, a wholly owned subsidiary of  
632 Honeywell International Inc., for the U.S. Department of Energy’s National Nuclear Secu-  
633 rity Administration under contract DE-NA0003525. This paper describes objective technical  
634 results and analysis. Any subjective views or opinions that might be expressed in the pa-  
635 per do not necessarily represent the views of the U.S. Department of Energy or the United  
636 States Government. This article has been co-authored by an employee of National Tech-  
637 nology & Engineering Solutions of Sandia, LLC under Contract No. DE-NA0003525 with  
638 the U.S. Department of Energy (DOE). The employee owns all right, title and interest  
639 in and to the article and is solely responsible for its contents. The United States Gov-  
640 ernment retains and the publisher, by accepting the article for publication, acknowledges  
641 that the United States Government retains a non-exclusive, paid-up, irrevocable, world-  
642 wide license to publish or reproduce the published form of this article or allow others to  
643 do so, for United States Government purposes. The DOE will provide public access to  
644 these results of federally sponsored research in accordance with the DOE Public Access Plan  
645 <https://www.energy.gov/downloads/doe-public-access-plan>.

## 646 A Technical Details

647 This appendix presents the technical details of the PIROM framework applied to the trans-  
 648ient modeling of thermo-ablative TPS. The first section provides the mathematical details  
 649 for the definition of the DG-FEM. The second section details the coarse-graining proce-  
 650 dures performed on the DG-FEM representation of the TPS. The third section presents the  
 651 derivation of the LCM model from an energy-conservation perspective.

### 652 A.1 Full-Order Model

653 To obtain the full-order numerical solution, the governing equation is spatially discretized  
 654 using variational principles of Discontinuous Galerkin (DG) to result in a high-dimensional  
 655 system of ordinary differential equations (ODEs). The DG-FEM model is written in an  
 656 element-wise form, which is beneficial for subsequent derivations of the lower-order models.  
 657 Note that the choice of DG approach here is mainly for theoretical convenience in the sub-  
 658 sequent coarse-graining formulation. In the numerical results, the full-order TPS ablation  
 659 simulations is computed using standard FEM instead, and the equivalence between DG and  
 660 standard FEM is noted upon their convergence.

#### 661 A.1.1 Domain Discretization

662 Consider a conforming mesh partition of the domain in Fig. 3, where each element belongs  
 663 to one and only one component. Denote the collection of all  $M$  elements as  $\{E_i\}_{i=1}^M$ . To ease  
 664 the description of the DG model, a graph structure is employed. The elements are treated  
 665 as vertices, the set of which is denoted  $\mathcal{V} = \{m\}_{m=1}^M$ . Two neighboring elements,  $E_i$  and  $E_j$ ,  
 666 are connected by an edge  $(i, j)$ , and the shared boundary between them is denoted  $e_{ij}$ . The  
 667 collection of all edges are denoted  $\mathcal{E}$ , and  $\mathcal{G}$  is referred to as a graph. In the graph, the edges  
 668 are unidirected, meaning if  $(i, j) \in \mathcal{E}$  then  $(j, i) \in \mathcal{E}$ . Furthermore, denote the neighbors  
 669 of the  $i$ -th element as  $\mathcal{N}_i = \{j | (i, j) \in \mathcal{E}\}$ . Lastly, for the ease of notation, introduce two  
 670 special indices:  $T$  for the boundary of an element that overlaps with the Dirichlet boundary  
 671 condition, and similarly  $q$  for the Neumann boundary condition.

#### 672 A.1.2 Weak Form of Discontinuous Galerkin Method

673 Choosing appropriate basis functions  $\phi_k$  and  $\phi_l$  and using the Interior Penalty Galerkin  
 674 (IPG) scheme [5], the variational bilinear form for Eq. (1a) is,

$$\sum_{i=1}^M a_{\epsilon,i}(\phi_k, \phi_l) = \sum_{i=1}^M L_i(\phi_k) \quad (52)$$

675 where  $\epsilon$  is an user-specified parameter and,

$$a_{\epsilon,i}(\phi_k, \phi_l) = \int_{E_i} \left( \rho c_p \phi_k \frac{\partial \phi_l}{\partial t} + \mathbf{k} \nabla \phi_k \cdot \nabla \phi_l - \rho c_p \phi_k \mathbf{v} \cdot \nabla \phi_l \right) dE_i \quad (53a)$$

$$\begin{aligned} & - \sum_{j \in \mathcal{N}_i \cup \{T_b\}} \int_{e_{ij}} \{ \mathbf{k} \nabla \phi_k \cdot n \} [\phi_l] de_{ij} + \epsilon \sum_{j \in \mathcal{N}_i \cup \{T_b\}} \int_{e_{ij}} \{ \mathbf{k} \nabla \phi_l \cdot n \} [\phi_k] de_{ij} \\ & + \sigma \sum_{j \in \mathcal{N}_i \cup \{T_b\}} \int_{e_{ij}} [\phi_k] [\phi_l] de_{ij} \end{aligned} \quad (53b)$$

$$L_i(v) = \epsilon \sum_{j \in \mathcal{N}_i \cup \{T_b\}} \int_{e_{ij}} (\mathbf{k} \nabla \phi_l \cdot n) T_b de_{ij} + \int_{e_{iq}} \phi_k q_b de_{iq} + \sigma \int_{e_{iT}} \phi_k T_b de_{iT} \quad (53c)$$

676 In the bi-linear form above, the notations  $[]$  and  $\{ \}$  are respectively the jumps and averages  
677 at the boundary  $e_{ij}$  share by two elements  $E_i$  and  $E_j$ ,

$$[u] = u|_{E_i} - u|_{E_j}, \quad \{u\} = \frac{1}{2} \left( u|_{E_i} + u|_{E_j} \right), \quad \text{for } x \in e_{ij} = E_i \cap E_j$$

678 Moreover, the terms associated with  $\sigma$  are introduced to enforce the Dirichlet boundary  
679 conditions;  $\sigma$  is a penalty factor whose value can depend on the size of an element. Depending  
680 on the choice of  $\epsilon$ , the bi-linear form corresponds to symmetric IPG ( $\epsilon = -1$ ), non-symmetric  
681 IPG ( $\epsilon = 1$ ), and incomplete IPG ( $\epsilon = 0$ ). All these schemes are consistent with the  
682 original PDE and have similar convergence rate with respect to mesh size. In the following  
683 derivations, the case  $\epsilon = 0$  is chosen for the sake of simplicity.

#### 684 A.1.3 Discontinuous Galerkin Model

685 Next, the DG-based model is written in an element-wise form. For the  $i$ -th element, use a  
686 set of  $P$  trial functions to represent the temperature as in ???. Without loss of generality,  
687 the trial functions are assumed to be orthogonal, so that,

$$\int_{E_i} \phi_l^i(x) \phi_k^i(x) d\Omega = 0, \quad l \neq k$$

688 where  $|E_i|$  is the area ( $n_d = 2$ ) or volume ( $n_d = 3$ ) of the  $i$ -th element, and  $\delta_{lk}$  is the Kronecker  
689 delta function. Furthermore, for simplicity, choose  $\phi_1^i = 1$ . Thus, by orthogonality,

$$\int_{E_i} \phi_1^i(x) d\Omega = |E_i|, \quad \int_{E_i} \phi_k^i(x) d\Omega = 0, \quad k = 2, 3, \dots, P$$

690 Under the choice of basis functions,  $u_1^i$  is simply the average temperature of element  $E_i$ ,  
691 denoted as  $\bar{u}_i$ .

692 Using test functions same as trial functions, the dynamics  $\mathbf{u}_i$  is obtained by evaluating  
693 the element-wise bi-linear forms,

$$a_{\epsilon,i}(\phi_k^i, T^i) = L_i(\phi_k^i), \quad k = 1, 2, \dots, P \quad (54)$$

<sup>694</sup> Therefore, by standard variational principles, e.g., [5], the element-wise governing equation  
<sup>695</sup> is denoted as,

$$\mathbf{A}^i \dot{\mathbf{u}}_i = (\mathbf{B}^i + \mathbf{C}^i) \mathbf{u}_i + \sum_{j \in \mathcal{N}_i \cup \{T_b\}} (\mathbf{B}_{ij}^i \mathbf{u}_i + \mathbf{B}_{ij}^j \mathbf{u}_j) + \mathbf{f}_i(t), \quad \text{for } i = 1, 2, \dots, M \quad (55)$$

<sup>696</sup> where for  $k, l = 1, 2, \dots, P$ ,

$$[\mathbf{A}^i]_{kl} = \int_{E_i} \rho c_p \phi_k^i \phi_l^i dE_i \quad (56a)$$

$$[\mathbf{B}^i]_{kl} = - \int_{E_i} (\nabla \phi_k^i) \cdot (\mathbf{k} \nabla \phi_l^i) dE_i \quad (56b)$$

$$[\mathbf{C}^i]_{kl} = \int_{E_i} \rho c_p \phi_k^i \mathbf{v}_m^i \cdot \nabla \phi_l^i dE_i \quad (56c)$$

$$[\mathbf{B}_{ij}^i] = \int_{e_{ij}} \{ \mathbf{k} \nabla \phi_k^i \cdot \hat{n} \} \phi_l^i - \sigma [\phi_k^i] \phi_l^i de_{ij} \quad (56d)$$

$$[\mathbf{B}_{ij}^j] = \int_{e_{ij}} - \{ \mathbf{k} \nabla \phi_k^i \cdot \hat{n} \} \phi_l^j + \sigma [\phi_k^i] \phi_l^j de_{ij} \quad (56e)$$

$$[\mathbf{f}^i]_k = \int_{e_{iq}} \phi_k^i q_b de_{iq} + \sigma \int_{e_{iT}} \phi_k^i de_{iT} \quad (56f)$$

<sup>697</sup> The matrices  $\mathbf{A}^i \in \mathbb{R}^{P \times P}$ ,  $\mathbf{B}^i \in \mathbb{R}^{P \times P}$ , and  $\mathbf{C}^i \in \mathbb{R}^{P \times P}$  are respectively the capacitance,  
<sup>698</sup> conductivity, and advection matrices for element  $i$ . These matrices depend on  $\rho$ ,  $c_p$ ,  $\mathbf{k}$ , and  
<sup>699</sup>  $\mathbf{v}$ , and hence can be non-linear functions of  $\mathbf{u}_i$ . Since the trial functions are orthogonal, if  
<sup>700</sup>  $\rho c_p$  is constant within an element,  $\mathbf{A}^i$  is diagonal; otherwise,  $\mathbf{A}^i$  is symmetric and positive  
<sup>701</sup> definite as  $\rho c_p > 0$ .

<sup>702</sup> For compactness, the element-wise model in Eq. (55) is also written in matrix form,

$$\mathbf{A} \dot{\mathbf{u}} = [\mathbf{B} + \mathbf{C}(\mathbf{u})] \mathbf{u} + \mathbf{f}(t) \quad (57)$$

<sup>703</sup> where  $\mathbf{u} = [\mathbf{u}^{(1)}, \mathbf{u}^{(2)}, \dots, \mathbf{u}^{(M)}]^T \in \mathbb{R}^{MP}$  includes all DG variables,  $\mathbf{f} = [\mathbf{f}^{(1)}, \mathbf{f}^{(2)}, \dots, \mathbf{f}^{(M)}]^T \in \mathbb{R}^{MP}$ ,  $\mathbf{A}$  and  $\mathbf{C}$  are matrices of  $M$  diagonal blocks whose  $i$ -th blocks are  $\mathbf{A}^i$  and  $\mathbf{C}^i$ , and  $\mathbf{B}$   
<sup>704</sup> is a matrix of  $M \times M$  blocks whose  $(i, j)$ -th block is,  
<sup>705</sup>

$$\mathbf{B}_{ij} = \begin{cases} \mathbf{B}^i + \sum_{j \in \mathcal{N}_i \cup \{T_b\}} \mathbf{B}_{ij}^i, & i = j \\ \mathbf{B}_{ij}^j, & i \neq j \end{cases} \quad (58)$$

<sup>706</sup> The dependency of  $\mathbf{C}$  on  $\mathbf{u}$  is explicitly noted in Eq. (57), which is the main source of  
<sup>707</sup> non-linearity in the current TPS problem. Moreover, the mesh velocity  $\mathbf{v}$  varies with space  
<sup>708</sup> and time, and thus the advection matrix  $\mathbf{C}$  varies with time as a function of the surface  
<sup>709</sup> temperature  $T_q(x, t)$ .

## 710 A.2 Coarse-Graining of Dynamics

711 The LCM is obtained by coarse-graining the full-order DG-FEM. This coarse-graining pro-  
 712 cedure produces resolved  $\mathbf{r}^{(1)}(\bar{\mathbf{u}}, t)$  and residual  $\mathbf{r}^{(2)}(\mathbf{u}, t)$  dynamics as in Eq. (24). This  
 713 section presents the detail derivations and magnitude analysis for the resolved and residual  
 714 dynamics.

### 715 A.2.1 Resolved Dynamics

716 Using Eq. (21), the resolved dynamics is computed as follows,

$$\mathbf{r}^{(1)}(\bar{\mathbf{u}}, t) = \mathcal{P} [\Phi^+ \mathbf{A}^{-1} (\mathbf{B}\mathbf{u} + \mathbf{C}(\mathbf{u})\mathbf{u} + \mathbf{f}(t))] \quad (59a)$$

$$= \Phi^+ \mathbf{A}^{-1} \mathbf{P} \mathbf{B} \mathbf{P} \mathbf{u} + \Phi^+ \mathbf{A}^{-1} \mathbf{P} \mathbf{C} (\mathbf{P} \mathbf{u}) \mathbf{P} \mathbf{u} + \Phi^+ \mathbf{A}^{-1} \mathbf{P} \mathbf{f}(t) \quad (59b)$$

$$= \underbrace{\Phi^+ \mathbf{A}^{-1} \Phi}_{\#1} \underbrace{\Phi^+ \mathbf{B} \Phi \bar{\mathbf{u}}}_{\#2} + \Phi^+ \mathbf{A}^{-1} \Phi \underbrace{\Phi^+ \mathbf{C} (\Phi \bar{\mathbf{u}}) \Phi}_{\#3} \bar{\mathbf{u}} + \Phi^+ \mathbf{A}^{-1} \Phi \underbrace{\Phi^+ \mathbf{f}(t)}_{\#4} \quad (59c)$$

717 Detailed derivations for the #1, #2, and #4 terms can be found in Ref. [18] for the case  
 718 of temperature-varying matrices, where it is shown that coarse-graining the capacitance,  
 719 conductivity, and forcing terms result exactly in the LCM matrices. The remaining term #3  
 720 is analyzed next.

721 **Term #3** The  $\mathbf{C}(\mathbf{u}) \in \mathbb{R}^{MP \times MP}$  matrix contains  $M$  diagonal of size  $P \times P$ , since the  
 722 basis functions are defined locally on each element. Therefore,  $[\mathbf{C}(\mathbf{u})]_{ij} = \mathbf{0}$  for all  $i \neq j$  with  
 723  $i, j = 1, 2, \dots, M$ . It follows that for  $k, l = 1, 2, \dots, N$ ,

$$[\Phi^+ \mathbf{C}(\Phi \bar{\mathbf{u}}) \Phi]_{kl} = \sum_{i=1}^M \sum_{j=1}^M \varphi_i^{k+} [\mathbf{C}(\Phi \bar{\mathbf{u}})]_{ij} \varphi_j^l \quad (60a)$$

$$= \sum_{i=1}^M \varphi_i^{k+} [\mathbf{C}(\Phi \bar{\mathbf{u}})]_{ii} \varphi_i^l \quad (60b)$$

$$= \sum_{i \in \mathcal{V}_k} \varphi_i^{k+} [\mathbf{C}(\Phi \bar{\mathbf{u}})]_{ii} \varphi_i^l \quad (60c)$$

724 where in the second row, the fact that  $[\mathbf{C}(\mathbf{u})]_{ij} = 0$  for all  $i \neq j$  is used, and in the last row,  
 725 the fact that  $\varphi_i^{k+} = 0$  for all  $i \notin \mathcal{V}_k$  is used. Now, considering that  $[\mathbf{C}(\mathbf{u})]_{ii}$  has a (1, 1)-th  
 726 zero element, i.e.,  $[C_{11}(\Phi \bar{\mathbf{u}})]_{ii} = 0$ , and that if  $k \neq l$  then  $i \notin \mathcal{V}_l$  and thus  $\varphi_i^l = \mathbf{0}$ , it follows  
 727 that for some index  $i \in \mathcal{V}_k$ ,

$$\varphi_i^{k+} [\mathbf{C}(\Phi \bar{\mathbf{u}})]_{ii} \varphi_i^l = \varphi_i^{k+} [\mathbf{C}(\Phi \bar{\mathbf{u}})]_{ii} \varphi_i^k = \frac{|E_i|}{|\Omega_k|} [C_{11}(\Phi \bar{\mathbf{u}})]_{ii} = 0 \quad (61)$$

728 The matrix  $[\Phi^+ \mathbf{C}(\Phi \bar{\mathbf{u}}) \Phi]_{kl} = 0$  for all  $k, l = 1, 2, \dots, N$ , and thus,

$$\bar{\mathbf{C}}(\bar{\mathbf{u}}) = \Phi^+ \mathbf{C}(\Phi \bar{\mathbf{u}}) \Phi = \mathbf{0} \quad (62)$$

729 as indicated by the LCM in Eq. (11).

### 730 A.2.2 Magnitude Analysis for Residual Dynamics

731 Next, the magnitude of the residual dynamics  $\mathbf{r}^{(2)}(\mathbf{u}, t)$  is analyzed to pinpoint the missing  
732 physics in the LCM. By definition,

$$\mathbf{r}^{(2)}(\mathbf{u}, t) = \dot{\bar{\mathbf{u}}} - \mathbf{r}^{(1)}(\bar{\mathbf{u}}, t) \quad (63a)$$

$$= \Phi^+ \mathbf{r}(\mathbf{u}, t) - \mathbf{r}^{(1)}(\bar{\mathbf{u}}, t) \quad (63b)$$

$$= \underbrace{\Phi^+ \mathbf{A}^{-1} \mathbf{B} \mathbf{u} - \bar{\mathbf{A}}(\mathbf{w})^{-1} \bar{\mathbf{B}}(\mathbf{w}) \bar{\mathbf{u}}}_{\#1} + \underbrace{\Phi^+ \mathbf{A}^{-1} \mathbf{C}(\mathbf{u}) \mathbf{u} - \bar{\mathbf{A}}(\mathbf{w})^{-1} \bar{\mathbf{C}}(\bar{\mathbf{u}}) \bar{\mathbf{u}}}_{\#2} \quad (63c)$$

$$+ \underbrace{\Phi^+ \mathbf{A}^{-1} \mathbf{f}(t) - \bar{\mathbf{A}}(\mathbf{w})^{-1} \bar{\mathbf{f}}(t)}_{\#3} \quad (63d)$$

733 The magnitude analysis for terms  $\#1$  and  $\#3$  can be found in Ref. [18] for temperature-  
734 varying material properties. The remaining term  $\#2$  is analyzed next. Let  $\mathbf{D}(\bar{\mathbf{u}}) = \mathbf{A}^{-1} \mathbf{P} \mathbf{C}(\Phi \bar{\mathbf{u}})$   
735 so that,

$$\Phi^+ \mathbf{A}^{-1} \mathbf{C}(\mathbf{u}) \mathbf{u} - \bar{\mathbf{A}}(\mathbf{w})^{-1} \bar{\mathbf{C}}(\bar{\mathbf{u}}) \bar{\mathbf{u}} \quad (64a)$$

$$= \Phi^+ \mathbf{A}^{-1} \mathbf{C}(\mathbf{u}) \mathbf{u} - \Phi^+ \mathbf{A}^{-1} \mathbf{P} \mathbf{C}(\Phi \bar{\mathbf{u}}) \Phi \Phi^+ \mathbf{u} \quad (64b)$$

$$= \Phi^+ \mathbf{A}^{-1} \mathbf{C}(\mathbf{u}) \mathbf{u} - \Phi^+ \mathbf{D}(\bar{\mathbf{u}}) \Phi \Phi^+ \mathbf{u} \quad (64c)$$

$$(64d)$$

736 where  $\mathbf{P} = \Phi \Phi^+$ . Thus,

$$\|\Phi^+ \mathbf{A}^{-1} \mathbf{C}(\mathbf{u}) \mathbf{u} - \bar{\mathbf{A}}(\mathbf{w})^{-1} \bar{\mathbf{C}}(\bar{\mathbf{u}}) \bar{\mathbf{u}}\| \quad (65a)$$

$$\leq \|\Phi^+ \mathbf{A}^{-1} \mathbf{C}(\mathbf{u}) \mathbf{u} - \Phi^+ \mathbf{D}(\bar{\mathbf{u}}) \mathbf{u}\| + \|\Phi^+ \mathbf{D}(\bar{\mathbf{u}}) \mathbf{u} - \Phi^+ \mathbf{D}(\bar{\mathbf{u}}) \Phi \Phi^+ \mathbf{u}\| \quad (65b)$$

$$\leq \|\Phi^+\| \underbrace{\|\mathbf{A}^{-1} \mathbf{C}(\mathbf{u}) \mathbf{u} - \mathbf{D}(\bar{\mathbf{u}}) \mathbf{u}\|}_{\#1} + \|\Phi^+ \mathbf{D}(\bar{\mathbf{u}})\| \underbrace{\|\mathbf{u} - \Phi \Phi^+ \mathbf{u}\|}_{\#2} \quad (65c)$$

737 Similar to the analysis in Ref. [18], term  $\#2$  is due to the approximation of non-uniform  
738 temperature as constants in each component, and the term  $\#1$  is the error in the advection  
739 effects due to such approximation.

### 740 A.3 Lumped Capacitance Model

741 The following assumptions are employed: (1) the temperature in the  $i$ -component is described  
742 by a scalar time-varying average temperature  $\bar{u}_i$ , (2) between neighboring components ( $i$ )  
743 and ( $j$ ) the heat flux is approximated as,

$$q_{ij} = \frac{\bar{u}_j - \bar{u}_i}{R_{ij}} \quad (66)$$

744 where  $R_{ij}$  is the thermal resistance. Empirically, for a component of isotropic heat conduction  
 745 conductivity  $k$ , length  $\ell$ , and cross-section area  $A$ , the thermal resistance is  $R = \ell/kA$ . Between  
 746 components  $i$  and  $j$ , define  $R_{ij} = R_i + R_j$ . In addition, the heat flux due to Dirichlet  
 747 boundary condition is computed as  $q_{iT} = (T_b - \bar{u}_i)/R_i$ .

748 At component  $i$ , the dynamics of LCM are given by,

$$\int_{E_i} \rho c_p \dot{\bar{u}}_i dE_i = \left( \sum_{j \in \mathcal{N}_i} \int_{e_{ij}} \frac{\bar{u}_j - \bar{u}_i}{R_{ij}} de_{ij} \right) + \int_{e_{iq}} q_b de_{iq} + \int_{e_{iT}} \frac{T_b - \bar{u}_i}{R_i} de_{iT} \quad (67a)$$

$$\bar{A}_i \dot{\bar{u}}_i = \left( \sum_{j \in \mathcal{N}_i} \frac{|e_{ij}|}{R_{ij}} (\bar{u}_j - \bar{u}_i) \right) + |e_{iq}| \bar{q}_i + \frac{|e_{iT}|}{R_i} (\bar{T}_i - \bar{u}_i) \quad (67b)$$

$$= \sum_{j \in \mathcal{N}_i} \left( -\frac{|e_{ij}|}{R_{ij}} \bar{u}_i + \frac{|e_{ij}|}{R_{ij}} \bar{u}_j \right) + \left( -\frac{|e_{iT}|}{R_i} \bar{u}_i \right) + \left( |e_{iq}| \bar{q}_i + \frac{|e_{iT}|}{R_i} \bar{T}_i \right) \quad (67c)$$

$$= \sum_{j \in \mathcal{N}_i \cup \{T_b\}} (\bar{B}_{ij}^i \bar{u}_i + \bar{B}_{ij}^j \bar{u}_j) + \bar{f}_i \quad (67d)$$

749 where in Eq. (67b)  $|e|$  denotes the length ( $d = 2$ ) or area ( $d = 3$ ) of a component boundary  
 750  $e$ . The  $\bar{A}_i$ ,  $\bar{B}_{ij}^i$ , and  $\bar{B}_{ij}^j$  quantities are provided in Eq. (14).

751 The lumped-mass representation for the four-component TPS is shown in Fig. 3. Let  
 752  $\mathbf{w} \in \mathbb{R}^{\tilde{N}}$  be the one-dimensional surface displacements of the ablative TPS components,  $v_i$   
 753 represent the area of the  $i$ -th component,  $\bar{\rho}c_{p,i}$ , the constant heat capacitance, and  $1/R_{ij} =$   
 754  $1/R_i + 1/R_j$  the equivalent thermal resistance between  $i$  and  $j$ . Note that the areas and  
 755 equivalent thermal resistances vary with  $\mathbf{w}$  due to ablation. Leveraging the formulas from  
 756 Eqs. (13) and (14), the LCM matrices are given by,

$$\bar{\mathbf{A}} = \begin{bmatrix} \bar{\rho}c_{p,1} v_1 & 0 & 0 & 0 \\ 0 & \bar{\rho}c_{p,2} v_2 & 0 & 0 \\ 0 & 0 & \bar{\rho}c_{p,3} v_3 & 0 \\ 0 & 0 & 0 & \bar{\rho}c_{p,4} v_4 \end{bmatrix}, \quad (68a)$$

$$\bar{\mathbf{B}} = \begin{bmatrix} \frac{1}{R_{12}} + \frac{1}{R_{14}} & -\frac{1}{R_{12}} & 0 & -\frac{1}{R_{14}} \\ -\frac{1}{R_{12}} & \frac{1}{R_{12}} + \frac{1}{R_{24}} + \frac{1}{R_{23}} & -\frac{1}{R_{23}} & -\frac{1}{R_{24}} \\ 0 & -\frac{1}{R_{32}} & \frac{1}{R_{32}} + \frac{1}{R_{34}} & -\frac{1}{R_{34}} \\ -\frac{1}{R_{14}} & -\frac{1}{R_{24}} & -\frac{1}{R_{34}} & \frac{1}{R_{14}} + \frac{1}{R_{24}} + \frac{1}{R_{34}} \end{bmatrix}, \quad \bar{\mathbf{f}} = \begin{bmatrix} \bar{q}^{(1)} \\ \bar{q}^{(2)} \\ \bar{q}^{(3)} \\ 0 \end{bmatrix} \quad (68b)$$

## 757 References

- [1] Adam J. Amar, A. Brandon Oliver, Benjamin S. Kirk, Giovanni Salazar, and Justin Drob. Overview of the charring ablator response (char) code. In AIAA, editor, *AIAA Aviation Forum*, 2016.
- [2] Guy L. Bergel, Frank B. Beckwith, Gabel J. de Frias, Kevin M. Manktelow, Mark T. Merewether, Scott T. Miller, Krishen J. Parmar, Timothy S. Shelton, Jesse T. Thomas,

- 763            Jeremy T. Trageser, Benjamin T. Treweek, Michael V. Veilleux, and Ellen B. Wagman.  
 764            *Sierra/SolidMechanics 5.6 User's Manual*, 2022.
- 765            [3] Ricky T. Q. Chen, Yulia Rubanova, Jesse Bettencourt, and David Duvenaud. Neural  
 766            ordinary differential equations, 2019.
- 767            [4] Jonathan Clausen, Victor Brunini, Lincoln Collins, Robert C Knaus, Alec Kucala,  
 768            Stephen Lin, Daniel Robert Moser, Malachi Phillips, Thomas Michael Ransegrenola,  
 769            Samuel Ramirez Subia, et al. Sierra multimechanics module: Aria verification manual-  
 770            version 5.22. Technical report, Sandia National Lab.(SNL-NM), Albuquerque, NM  
 771            (United States), 2024.
- 772            [5] Gary Cohen and Sebastien Pernet. *Finite Element and Discontinuous Galerkin Methods  
 773            for Transient Wave Equations*. Springer Dordrecht, Le Chesnay and Toulouse France,  
 774            2018.
- 775            [6] Jianhao Fang, Weifei Hu, Zhenyu Liu, Yuhao Zhou, Chao Wei, and Jianrong Tan. A  
 776            reduced order finite element-informed surrogate model for approximating global high-  
 777            fidelity simulations. *Structural and Multidisciplinary Optimization*, 67(12), 2024.
- 778            [7] Matthew Gasch, Keith Peterson, Mairead Stackpoole, Ethiraj Venkatapathy, Gregory  
 779            Gonzales, and Kyle Hendrickson. Development of advanced ablative carbon phenolic  
 780            tps for future nasa missions and commercial space. In *38th Annual Small Satellite  
 781            Conference*, Logan, Utah, May 2024.
- 782            [8] Micah A. Howard and Ben F. Blackwell. A multi-dimensional finite element based solver  
 783            for decomposing and non-decomposing thermal protection systems. In AIAA, editor,  
 784            *AIAA Aviation Forum*, 2015.
- 785            [9] Frank P. Incropera, David P. DeWitt, Theodore L. Bergman, and Adrienne S. Lavine.  
 786            *Fundamentals of Heat and Mass Transfer*. Wiley, Hoboken, NJ, 7th edition, 2011.
- 787            [10] R. J. Klock and Carlos Cesnik. Nonlinear thermal reduced-order modeling for hypersonic  
 788            vehicles. *AIAA Journal*, 55(7), 2017.
- 789            [11] Arun Govind Neelan. Linear and non-linear reduced order model of scramjet. In *Ad-  
 790            vances in Multidisciplinary Design, Analysis and Optimization*, pages 111–118, Singa-  
 791            pore, 2025.
- 792            [12] Alberto Padovan, Blaine Vollmer, Francesco Panerai, Marco Panesi, Kelly A. Stephani,  
 793            and Daniel J. Bodony. An extended bformulation for ablating-surface boundary condi-  
 794            tions. *International Journal of Heat and Mass Transfer*, 218:124770, 2024.
- 795            [13] Eric Parish and Karthik Duraisamy. Non-markovian closure models for large eddy  
 796            simulations using the mori-zwanzig formalism. *Phys. Rev. Fluids*, 2:014604, Jan 2017.
- 797            [14] Eric Parish and Karthik Duraisamy. A unified framework for multiscale modeling using  
 798            the mori-zwanzig formalism and the variational multiscale method. *ArXiv*, 12 2017.

- 799 [15] Eric Parish and Karthik Duraisamy. *Coarse-Graining Turbulence Using the*  
800 *Mori-Zwanzig Formalism*. Cambridge University Press, Cambridge, 2025.
- 801 [16] Carl Edward Rasmussen and Christopher K. I. Williams. *Gaussian Processes for Ma-*  
802 *chine Learning*. The MIT Press, 2006.
- 803 [17] Adam Thelen, Xiaoge Zhang, Olga Fink, Yan Lu, Sayan Ghosh, Byeng D. Youn,  
804 Michael D. Todd, Sankaran Mahadean, Chao Hu, and Zhen Hu. A comprehensive  
805 review of digital twin – part 1: modeling and twinning enabling technologies. *Structural*  
806 *and Multidisciplinary Optimization*, 65(12), 2022.
- 807 [18] Carlos A. Vargas Venegas, Daning Huang, Patrick Blonigan, and JohnTencer. Physics-  
808 infused reduced-order modeling for analysis of multi-layered hypersonic thermal protec-  
809 tion systems, 2025.
- 810 [19] Yongyong Xian, Baisong Pan, and Luping Luo. A new model updating strategy with  
811 physics-based and data-driven models. *Structural and Multidisciplinary Optimization*,  
812 64(1), 2021.
- 813 [20] Yin Yu, John Harlim, Daning Huang, and Yan Li. Learning coarse-grained dynamics  
814 on graph. *arXiv preprint arXiv:2405.09324*, 2024.